Atmospheric new particle formation from sulfuric acid and amines in a Chinese megacity

Yao, Lei; Garmash, Olga; Bianchi, Federico; Zheng, Jun; Yan, Chao ...

2018-07-20

American association for the advancement of science

http://hdl.handle.net/10138/309487

Yao, L, Garmash, O, Bianchi, F, Zheng, J, Yan, C, Kontkanen, J, Junninen, H, Mazon, S B, Ehn, M, Paasonen, P, Sipilä, M, Wang, M, Wang, X, Xiao, S, Chen, H, Lu, Y, Zhang, B, Wang, D, Fu, Q, Geng, F, Li, L, Wang, H, Qiao, L, Yang, X, Chen, J, Kerminen, V-M, Petäjä, T, Worsnop, D R, Kulmala, M & Wang, L 2018, 'Atmospheric new particle formation from sulfuric acid and amines in a Chinese megacity', Science, vol. 361, no. 6399, pp. 278-281. https://doi.org/10.1126/science.aao4839

Title: Atmospheric New Particle Formation from Sulfuric Acid and Amines in a Chinese Megacity

Authors: Lei Yao[1,§], Olga Garmash[2,§], Federico Bianchi[2], Jun Zheng[3], Chao Yan[2], Jenni Kontkanen[2,4], Heikki Junninen[2], Stephany Buenrostro Mazon[2], Mikael Ehn[2], Pauli Paasonen[2], Mikko Sipilä[2], Mingyi Wang[1,a], Xinke Wang[1], Shan Xiao[1,b], Hangfei Chen[1], Yiqun Lu[1], Bowen Zhang[1], Dongfang Wang[5], Qingyan Fu[5], Fuhai Geng[6], Li Li[7], Hongli Wang[7], Liping Qiao[7], Xin Yang[1,8,9], Jianmin Chen[1,8,9], Veli-Matti Kerminen[2], Tuukka Petäjä[2], Douglas R. Worsnop[10], Markku Kulmala[2], Lin Wang[1,8,9,11*]

Affiliations:

[1] Shanghai Key Laboratory of Atmospheric Particle Pollution and Prevention (LAP[3]), Department of Environmental Science & Engineering, Fudan University, Shanghai 200433, China

[2] Institute for Atmospheric and Earth System Research / Physics, Faculty of Science, University of Helsinki, Helsinki, 00014, Finland

[3]Jiangsu Key Laboratory of Atmospheric Environment Monitoring and Pollution Control, Nanjing University of Information Science & Technology, Nanjing 210044, China

[4] Department of Environmental Science and Analytical Chemistry (ACES) & Bolin Centre for Climate Research, Stockholm University, 10691 Stockholm, Sweden

[5] Shanghai Environmental Monitoring Center, Shanghai 200030, China

[6] Shanghai Meteorology Bureau, Shanghai 200135, China

[7] Shanghai Academy of Environmental Sciences, Shanghai 200233, China

[8] Institute of Atmospheric Sciences, Fudan University, Shanghai 200433, China

[9] Collaborative Innovation Center of Climate Change, Nanjing 210023, China

[10] Aerodyne Research, Inc., Billerica, MA 01821, USA

[11] Shanghai institute of pollution control and ecological security, Shanghai 200092, China

[a] now at: Center for Atmospheric Particle Studies, Carnegie Mellon University, Pittsburgh, PA 15213, USA

[b] now at: Shanghai Qingning Environmental Planning & Design Co. Ltd, Shanghai 200052, China

[*]Corresponding author: lin_wang@fudan.edu.cn

[§]These authors contributed equally to this work.

Abstract: Atmospheric new particle formation (NPF) is a global and important phenomenon that is yet extremely sensitive to ambient conditions. According to both observation and theoretical arguments, NPF usually requires a relatively high H_2SO_4 concentration to promote the formation of new particles and a low pre-existing aerosol loading to minimize the sink of new particles. Here, we investigated NPF in Shanghai and were able to observe both precursor vapors (H_2SO_4) and initial clusters at a molecular level in a megacity. High new particle formation rates were observed to

coincide with several familiar markers suggestive of H_2SO_4-dimethylamine (DMA)-H_2O nucleation, including sulfuric acid dimers and H_2SO_4-DMA clusters. Based on cluster kinetics simulation, the observed concentration of sulfuric acid was high enough to explain the growth to around 3 nm under the very high condensation sink, whereas the subsequent faster growth rate above this size is believed to result from the added contribution of condensing organic species. These findings will help to understand urban NPF and its air quality and climate impact as well as to formulate policies to mitigate secondary particle formation in China.

One Sentence Summary:
New particle formation in a Chinese megacity proceeds via the sulfuric acid-dimethylamine-water, acid-base nucleation mechanism and it is an important source of urban aerosol particles in terms of number concentration.

Main Text:
Atmospheric nucleation and subsequent growth of newly formed particles are a major source of atmospheric aerosol particles in terms of their number concentration (*1-4*), which can affect our climate directly and indirectly (*5*). During the past several years, our knowledge on new particle formation (NPF) has dramatically increased through laboratory experiments, especially those carried out in the Cosmics Leaving OUtdoor Droplets (CLOUD) chamber at CERN (*6-11*). Detailed mechanisms for atmospheric nucleation have been proposed for a few locations with low background aerosol loadings (*8,12-14*).

It is still a puzzle why and how NPF occurs in a highly-polluted urban atmosphere like in Chinese megacities (*15,16*). The very high aerosol concentration, causing a large condensation sink (CS), should efficiently scavenge newly-formed molecular clusters before they reach sizes of a few nanometers, except when the cluster growth rate is exceptionally high (*15,17,18*). However, even in highly polluted areas like in Nanjing in Eastern China, the contribution of secondary aerosol production to the total aerosol number load is dominating and even more than half of accumulation mode aerosol particles have been estimated to be of secondary origin (*19*). The observation of frequent NPF events in megacities such as Beijing (*20,21*), Shanghai (*22*), and Nanjing (*23*) urges a major advance in our understanding of the physical and chemical mechanisms for NPF in a heavily-polluted atmosphere, which would ultimately help us to improve the performance of global and regional models.

Here we performed measurements in a Chinese megacity, Shanghai (fig. S1), in order to investigate the mechanisms and impacts of atmospheric NPF. The first data set includes long-term continuous observations between March 2014 and February 2016 of particle number size distributions down to about 1.2 nm and atmospheric trace gas concentrations. The instruments used during this period were one particle size magnifier (PSM), one nano scanning mobility particle sizer (nano-SMPS) and one long-SMPS. The second set of data were recorded during an intensive campaign from

December 2015 to February 2016 with additional mass spectrometric measurements of gas-phase aerosol precursors and clusters. During this period, we additionally used one Neutral cluster and Air Ion Spectrometer (NAIS) and one nitrate-based Chemical Ionization - Atmospheric Pressure interface - Time-of-Flight (CI-APi-TOF) Mass Spectrometer (*24*). These two complementary data sets provide both precise fingerprint-type details and the nucleation climatology that together elucidate the chemical and physical mechanisms for the observed NPF events.

During the long-term measurements, we identified 114 strong NPF events, with maximum-to-background concentration ratios > 20 for sub-3 nm particles, corresponding to a NPF frequency of 15.6%. As shown in table S1, particle formation rates ($J_{1.7}$) and CS in urban Shanghai are one to two orders of magnitude larger than typical values in the clean atmosphere (*15,22*). NPF events in urban Shanghai are favored on days with stronger solar radiation, higher ozone concentration, higher sulfuric acid concentration, lower relative humidity, and less NO_x (fig. S2). The correlation with radiation, sulfuric acid and ozone production indicates that the identified NPF events in Shanghai were generally photo-chemically induced. Lower relative humidity is related to sunny days with strong radiation, which favor the formation of OH radical and hence sulfuric acid (*25*). NO_x can react with peroxy radicals to compete with the autoxidation pathway, thereby hindering the formation of critical intermediates for NPF (*26*).

When looking at NPF at a molecular level, we found that naturally-charged 2-4 nm ions (figs. S3b & S4) were scavenged by pre-existing particles in Shanghai, providing little information except that ion-induced nucleation was not responsible for the observed NPF events. The ion-induced contribution to NPF based on the calculated ratio of $J_{1.7}$-(ion)/$J_{1.7}$(total) was 0.03% for negative ions and 0.05% for positive ions, respectively. We therefore concentrated on neutral compounds and clusters measured using a nitrate-based CI-APi-TOF during the intensive campaign. The most striking observation was the highest signal of sulfuric acid dimer, $H_2SO_4 \cdot HSO_4^-$, ever observed in an ambient atmosphere (see also Kürten et al. (*27*)). $H_2SO_4 \cdot HSO_4^-$ detected by the nitrate-based CI-APi-TOF has previously been explained by the stabilization of the neutral sulfuric acid dimer in the real atmosphere by dimethylamine (DMA) (*6,9,28*) or by a molecule that works in the same way as DMA. During the charging process by the NO_3^- reagent ions, DMA evaporated and one H_2SO_4 was replaced with one bisulfate ion HSO_4^-. Particle formation rate against measured $H_2SO_4 \cdot HSO_4^-$ is shown in Fig. 1A. A good correlation ($r = 0.75$, p-value < 0.001) is evident for the dimer concentration exceeding 1×10^4 cm^{-3}. This suggests that the formation of atmospheric clusters giving a strong sulfuric acid dimer signal in the CI-APi-TOF was crucial for the observed nucleation processes.

Figure 1B presents the median sulfuric acid dimer concentration as a function of sulfuric acid monomer concentration for NPF and non-event days during the intensive campaign. Our measured dimer-to-monomer ratio is much larger than the corresponding theoretical maximum ratio due to ion-induced clustering (IIC) of sulfuric

acid within the CI-APi-TOF ion reaction zone (*29*), being about one order of magnitude larger than previously reported ambient values when sulfuric acid monomer concentration reached 1×10^7 molecule cm^{-3} (*27,29*). At this level of sulfuric acid concentration, our dimer-to-monomer ratio is close to a previous experimental observation from H_2SO_4-DMA-H_2O nucleation in the CLOUD experiment (*9*). Cluster kinetics simulations (see Supplementary Materials) for a kinetically-limited H_2SO_4-DMA system show a qualitative agreement with our measured values including the effect of CS on the dimer-to-monomer ratio (Fig.1B). During NPF days, this ratio is larger and the CS is smaller, which is opposite to non-event days. It seems that very high CS values (> 0.02 s^{-1}) will prevent new particle formation in Shanghai. However, already the values of around 0.01-0.02 s^{-1} with observed growth rates are expected to cause very high scavenging of small clusters, indicating that our knowledge is still incomplete under polluted conditions (*15*).

As suggested by other neutral clusters (Fig. 1C), the identity of the stabilizer for sulfuric acid dimer is most likely DMA. We observed large sulfuric acid clusters (trimer and tetramer) and sulfuric acid-DMA clusters consisting of up to four molecules of sulfuric acid and two molecules of DMA in the ambient atmosphere, using nitrate-based CI-APi-TOF. However, since one or more DMA molecule(s) could have evaporated after the charging of the parent neutral sulfuric acid-DMA cluster by reagent ions (*6,9,30*), we expect a larger number of DMA molecules in sulfuric acid-DMA clusters than observed here. On the other hand, the fast particle growth rates in Shanghai corresponded to an almost simultaneous appearance of sulfuric acid clusters and sulfuric acid-DMA clusters. Nevertheless, the presence of sulfuric acid clusters and sulfuric acid-DMA clusters suggest that the initial growth of neutral clusters proceeded by addition of precursor gases or preformed clusters (*6*). Apart from these clusters, a large number of organic species were observed, including highly oxygenated molecules (HOMs) (*31*) (table S2). Due to the extreme chemical complexity of organic species in the urban atmosphere, we were only able to unambiguously assign molecular formulas to a few of them, likely formed by reactions of peroxy radicals with NO_x or autoxidation of peroxy radicals.

The measured particle formation rates give further support for the involvement of DMA, instead of any other stabilizer, in the observed NPF events. Figure 2 shows $J_{1.7}$ against the measured [H_2SO_4] and compares them to those measured for the H_2SO_4-H_2O, H_2SO_4-NH_3-H_2O, and H_2SO_4-DMA-H_2O nucleation mechanisms in the CERN-CLOUD experiments. Our measured particle formation rates are far higher than those derived from H_2SO_4-H_2O or H_2SO_4-NH_3-H_2O mechanisms (*10,27*), but close to those observed in the H_2SO_4-DMA-H_2O experiments (*9*). The average temperature (278±8 K) and relative humidity (36±7%) on the NPF days during the intensive campaign are close to the CLOUD experimental conditions (278 K and 38% RH) and hence temperature and relative humidity are not expected to significantly enhance the particle formation rates during this period in Shanghai (*32*). The average concentration of C_2-amines was measured to be 40±14 pptv (parts per trillion by volume) in summer 2015

at the same sampling site (*33*), so the DMA concentration could have reached 5 pptv during the intensive campaign, a threshold value to hit the rate limit for H_2SO_4-DMA-H_2O ternary nucleation (*9*). A similar plot for the long-term measurements using calculated [H_2SO_4] (fig. S6) also points towards the H_2SO_4-DMA-H_2O nucleation. Moreover, our NPF observation during periods with measured DMA and calculated [H_2SO_4] also indicates the important roles of H_2SO_4 and DMA in NPF (figs. S7 & S8).

We measured growth rates (GR) of clusters and nanoparticles during the NPF events. Figure 3 shows that the GR of clusters and nanoparticles during intensive campaign increased steeply with their increasing size up to 25 nm, which is consistent with the observations from long-term measurements (Fig. S9). We performed cluster kinetics simulations for a collision-limited H_2SO_4-DMA system (*34*) using median sulfuric acid concentration and CS for the NPF events observed during the intensive campaign. The sub-3 nm GR determined from simulations is on average higher than the measured GR, which means that the sulfuric acid concentrations are sufficient to explain the observed growth of sub-3 nm particles considering that there is always a neutralizing base to stabilize sulfuric acid clusters (for instance, DMA). However, subsequent growth between 3 and 25 nm needs to be considerably boosted by organic vapors (*35*), some of which are likely detected with the CI-APi-TOF and some that are not (Fig. S10). With the typical values of GR observed in Shanghai, newly formed particles reach cloud condensation nuclei (CCN) sizes within a day.

Based on our calculations, the number of particles produced in NPF events is *ca.* 4.8 $\times 10^{21}$ km^{-2} $year^{-1}$ in the Shanghai area (see Supplementary Materials). This estimate is based only on the strongest NPF events and therefore the actual value is expected to be larger. Even so, this estimate is close to the estimates of anthropogenic primary aerosol emissions (2×10^{22} km^{-2} $year^{-1}$) within the most polluted part of Shanghai area (emission pixel 0.5 deg × 0.5 deg), and the average (5×10^{21} km^{-2} $year^{-1}$) in the somewhat larger area (1.5 deg × 1.5 deg) (*36*) (fig. S11). Direct comparison of our results with these estimates of primary anthropogenic particle number emissions suggests that the NPF contribution to the total aerosol number production is about 20% in the most polluted area and 50% in a wider urban environment. However, it is notable that, according to Paasonen et al. (2016) (*36*), also the anthropogenic particle number emissions are highly uncertain. The authors estimated that anthropogenic emissions of nucleation mode particles are in general underestimated due to the incomplete representation of the volatile primary particles in some of observational data applied for deriving the emission factors. Due to the mentioned probable underestimation in and uncertainties related to both the NPF and the anthropogenic particle number sources, this comparison should not be taken as an estimate of the exact shares of the sources, but as an indication that neither of them clearly dominates over the other.

In summary, we have performed a molecular level study of NPF events in a Chinese megacity. We detected high concentrations of sulfuric acid dimers, which points to strong acid-base stabilization in H_2SO_4-DMA clusters. When compared to CLOUD

measurements, the observed cluster formation events during our intensive campaign were consistent with H_2SO_4-DMA-H_2O nucleation, even though other mechanisms involving for example organic compounds could not be ruled out. Within experimental uncertainties, the sulfuric acid concentrations were high enough to result in the observed growth of sub-3 nm particles, provided that neutralizing bases, such as DMA, stabilized the sulfuric acid clusters. The exact contribution of organics and NH_3 to the growth of large clusters is yet to be elucidated. Although our results provide strong evidence for H_2SO_4-DMA-H_2O nucleation, it remains unclear how newly-formed molecular clusters are able to reach sizes of a few nanometers under high CS (fig. S12) unless molecular clusters are scavenged by pre-existing particles less efficiently than expected or growth rates are underestimated with our current methods (*15*).

Clearly, the strong atmospheric NPF in China is a result of the vast emissions of precursor gases. NPF events in turn lead to the formation of large concentrations of new atmospheric particles that have an impact on regional air quality and potentially also the regional and global climate. For example, in the Yangtze River delta where Shanghai is located, the emissions of precursor gases including sulfur dioxide, ammonia, and volatile organic compounds are extremely high (*37*). In addition, the concentrations of amines (*33,38*) are sufficient to allow sulfuric acid particles to form at their maximum (kinetically-limited) rate. Correspondingly, frequent atmospheric NPF is observed in this region (*22,23*). Hence, in order to reduce secondary aerosol formation in China, it is crucial to control the emissions of precursor compounds for new particle formation.

References and notes:

1. E.M. Dunne, H. Gordon, A.Kürten, J.Almeida, J. Duplissy, C.Williamson, I. K. Ortega, K. J. Pringle, A. Adamov, U. Baltensperger, P. Barmet, F. Benduhn, F. Bianchi, M. Breitenlechner, A. Clarke, J. Curtius, J. Dommen, N. M. Donahue, S. Ehrhart, R. C. Flagan, A. Franchin, R. Guida, J. Hakala, A. Hansel, M. Heinritzi, T. Jokinen, J. Kangasluoma, J. Kirkby, M. Kulmala, A. Kupc, M. J. Lawler, K. Lehtipalo, V. Makhmutov, G. Mann, S. Mathot, J. Merikanto, P. Miettinen, A. Nenes, A. Onnela, A. Rap, C. L. S. Reddington, F. Riccobono, N. A. D. Richards, M. P. Rissanen, L. Rondo, N. Sarnela, S. Schobesberger, K. Sengupta, M. Simon, M. Sipilä, J. N. Smith, Y. Stozkhov, A. Tomé, J. Tröstl, P. E. Wagner, D. Wimmer, P. M. Winkler, D. R. Worsnop, K. S. Carslaw, Global atmospheric particle formation from CERN CLOUD measurements. *Science* **354**, 1119-1124 (2016). doi: 10.1126/science.aaf2649
2. D. V. Spracklen, K. S. Carslaw, J. Merikanto, G. W. Mann, C. L. Reddington, S. Pickering, J. A. Ogren, E. Andrews, U. Baltensperger, E. Weingartner, M. Boy, M. Kulmala, L. Laakso, H. Lihavainen, N. Kivekäs, M. Komppula, N. Mihalopoulos, G. Kouvarakis, S. G. Jennings, C. O'Dowd, W. Birmili, A. Wiedensohler, R. Weller, J. Gras, P. Laj, K. Sellegri, B. Bonn, R. Krejci, A. Laaksonen, A. Hamed, A. Minikin, R. M. Harrison, R. Talbot, J. Sun, Explaining global surface aerosol number concentrations in terms of primary emissions and particle formation. *Atmos. Chem. Phys.* **10**, 4775-4793, (2010). doi:10.5194/acp-10-4775-2010
3. F. Yu, G. Luo, Simulation of particle size distribution with a global aerosol model: contribution

of nucleation to aerosol and CCN number concentrations, *Atmos. Chem. Phys.*, **9**, 7691-7710 (2009).

4. M. Chen, M. Titcombe, J. K. Jiang, C. Jen, C. A. Kuang, M. L. Fischer, F. L. Eisele, J. I. Siepmann, D. R. Hanson, J. Zhao, P. H. McMurry, Acid-base chemical reaction model for nucleation rates in the polluted atmospheric boundary layer. *Proc. Natl. Acad. Sci. U.S.A.*, **109** (46), 18713-18718 (2012).
5. IPCC. *IPCC, 2013: Climate change 2013: The physical science basis*. (Cambridge University Press, United Kingdom and New York, NY, USA, 2013).
6. A. Kürten, T. Jokinen, M. Simon, M. Sipilä, N. Sarnela, H. Junninen, A. Adamov, J. Almeida, A. Amorim, F. Bianchi, M. Breitenlechner, J. Dommen, N. M. Donahue, J. Duplissy, S. Ehrhart, R. C. Flagan, A. Franchin, J. Hakala, A. Hansel, M. Heinritzi, M. Hutterli, J. Kangasluoma, J. Kirkby, A. Laaksonen, K. Lehtipalo, M. Leiminger, V. Makhmutov, S. Mathot, A. Onnela, T. Petäjä, A. P. Praplan, F. Riccobono, M. P. Rissanen, L. Rondo, S. Schobesberger, J. H. Seinfeld, G. Steiner, A. Tomé, J. Tröstl, P. M. Winkler, C. Williamson, D. Wimmer, P. Ye, U. Baltensperger, K. S. Carslaw, M. Kulmala, D. R. Worsnop, J. Curtius, Neutral molecular cluster formation of sulfuric acid-dimethylamine observed in real time under atmospheric conditions. *Proc. Natl. Acad. Sci. USA* **111**, 15019-15024 (2014). doi: 10.1073/pnas.1404853111
7. F. Riccobono, S. Schobesberger, C. E. Scott, J. Dommen, I. K. Ortega, L. Rondo, J. Almeida, A. Amorim, F. Bianchi, M. Breitenlechner, A. David, A. Downard, E. M. Dunne, J. Duplissy, S. Ehrhart, R. C. Flagan, A. Franchin, A. Hansel, H. Junninen, M. Kajos, H. Keskinen, A. Kupc, A. Kürten, A. N. Kvashin, A. Laaksonen, K. Lehtipalo, V. Makhmutov, S. Mathot, T. Nieminen, A. Onnela, T. Petäjä, A. P. Praplan, F. D. Santos, S. Schallhart, J. H. Seinfeld, M. Sipilä, D. V. Spracklen, Y. Stozhkov, F. Stratmann, A. Tomé, G. Tsagkogeorgas, P. Vaattovaara, Y. Viisanen, A. Vrtala, P. E. Wagner, E. Weingartner, H. Wex, D. Wimmer, K. S. Carslaw, J. Curtius, N. M. Donahue, J. Kirkby, M. Kulmala, D. R. Worsnop, U. Baltensperger, Oxidation products of biogenic emissions contribute to nucleation of atmospheric particles. *Science* **344**, 717-721 (2014). Medline doi:10.1126/science.1243527
8. S. Schobesberger, H. Junninen, F. Bianchi, G. Lönn, M. Ehn, K. Lehtipalo, J. Dommen, S. Ehrhart, I. K. Ortega, A. Franchin, T. Nieminen, F. Riccobono, M. Hutterli, J. Duplissy, J. Almeida, A. Amorim, M. Breitenlechner, A. J. Downard, E. M. Dunne, R. C. Flagan, M. Kajos, H. Keskinen, J. Kirkby, A. Kupc, A. Kürten, T. Kurtén, A. Laaksonen, S. Mathot, A. Onnela, A. P. Praplan, L. Rondo, F. D. Santos, S. Schallhart, R. Schnitzhofer, M. Sipilä, A. Tomé, G. Tsagkogeorgas, H. Vehkamäki, D. Wimmer, U. Baltensperger, K. S. Carslaw, J. Curtius, A. Hansel, T. Petäjä, M. Kulmala, N. M. Donahue, D. R. Worsnop, Molecular understanding of atmospheric particle formation from sulfuric acid and large oxidized organic molecules. *Proc. Natl. Acad. Sci. USA* **110**, 17223-17228 (2013). Medline doi:10.1073/pnas.1306973110
9. J. Almeida, S. Schobesberger, A. Kürten, I. K. Ortega, O. Kupiainen-Määttä, A. P. Praplan, A. Adamov, A. Amorim, F. Bianchi, M. Breitenlechner, A. David, J. Dommen, N. M. Donahue, A. Downard, E. Dunne, J. Duplissy, S. Ehrhart, R. C. Flagan, A. Franchin, R. Guida, J. Hakala, A. Hansel, M. Heinritzi, H. Henschel, T. Jokinen, H. Junninen, M. Kajos, J. Kangasluoma, H. Keskinen, A. Kupc, T. Kurtén, A. N. Kvashin, A. Laaksonen, K. Lehtipalo, M. Leiminger, J. Leppä, V. Loukonen, V. Makhmutov, S. Mathot, M. J. McGrath, T. Nieminen, T. Olenius, A. Onnela, T. Petäjä, F. Riccobono, I. Riipinen, M. Rissanen, L. Rondo, T. Ruuskanen, F. D. Santos, N. Sarnela, S. Schallhart, R. Schnitzhofer, J. H. Seinfeld, M. Simon, M. Sipilä, Y. Stozhkov, F.

Stratmann, A. Tomé, J. Tröstl, G. Tsagkogeorgas, P. Vaattovaara, Y. Viisanen, A. Virtanen, A. Vrtala, P. E. Wagner, E. Weingartner, H. Wex, C. Williamson, D. Wimmer, P. Ye, T. Yli-Juuti, K. S. Carslaw, M. Kulmala, J. Curtius, U. Baltensperger, D. R. Worsnop, H. Vehkamäki, J. Kirkby, Molecular understanding of sulphuric acid-amine particle nucleation in the atmosphere. *Nature* **502**, 359-363 (2013). Medline doi:10.1038/nature12663

10. J. Kirkby, J. Curtius, J. Almeida, E. Dunne, J. Duplissy, S. Ehrhart, A. Franchin, S. Gagné, L. Ickes, A. Kürten, A. Kupc, A. Metzger, F. Riccobono, L. Rondo, S. Schobesberger, G. Tsagkogeorgas, D. Wimmer, A. Amorim, F. Bianchi, M. Breitenlechner, A. David, J. Dommen, A. Downard, M. Ehn, R. C. Flagan, S. Haider, A. Hansel, D. Hauser, W. Jud, H. Junninen, F. Kreissl, A. Kvashin, A. Laaksonen, K. Lehtipalo, J. Lima, E. R. Lovejoy, V. Makhmutov, S. Mathot, J. Mikkilä, P. Minginette, S. Mogo, T. Nieminen, A. Onnela, P. Pereira, T. Petäjä, R. Schnitzhofer, J. H. Seinfeld, M. Sipilä, Y. Stozhkov, F. Stratmann, A. Tomé, J. Vanhanen, Y. Viisanen, A. Vrtala, P. E. Wagner, H. Walther, E. Weingartner, H. Wex, P. M. Winkler, K. S. Carslaw, D. R. Worsnop, U. Baltensperger, M. Kulmala, Role of sulphuric acid, ammonia and galactic cosmic rays in atmospheric aerosol nucleation. *Nature* **476**, 429-433 (2011). Medline doi:10.1038/nature10343

11. J. Kirkby, J. Duplissy, K. Sengupta, C. Frege, H. Gordon, C. Williamson, M. Heinritzi, M. Simon, C. Yan, J. Almeida, J. Tröstl, T. Nieminen, I. K. Ortega, R. Wagner, A. Adamov, A. Amorim, A.-K. Bernhammer, F. Bianchi, M. Breitenlechner, S. Brilke, X. Chen, J. Craven, A. Dias, S. Ehrhart, R. C. Flagan, A. Franchin, C. Fuchs, R. Guida, J. Hakala, C. R. Hoyle, T. Jokinen, H. Junninen, J. Kangasluoma, J. Kim, M. Krapf, A. Kürten, A. Laaksonen, K. Lehtipalo, V. Makhmutov, S. Mathot, U. Molteni, A. Onnela, O. Peräkylä, F. Piel, T. Petäjä, A. P. Praplan, K. Pringle, A. Rap, N. A. D. Richards, I. Riipinen, M. P. Rissanen, L. Rondo, N. Sarnela, S. Schobesberger, C. E. Scott, J. H. Seinfeld, M. Sipilä, G. Steiner, Y. Stozhkov, F. Stratmann, A. Tomé, A. Virtanen, A. L. Vogel, A. Wagner, P. E. Wagner, E. Weingartner, D. Wimmer, P. M. Winkler, P. Ye, X. Zhang, A. Hansel, J. Dommen, N. M. Donahue, D. R. Worsnop, U. Baltensperger, M. Kulmala, K. S. Carslaw, J. Curtius, Ion-induced nucleation of pure biogenic particles. *Nature* **533**, 521-526, (2016). doi:10.1038/nature17953

12. F. Bianchi, J. Tröstl, H. Junninen, C. Frege, S. Henne, C.R. Hoyle, U. Molteni, E. Herrmann, A.Adamov, N. Bukowiecki, X. Chen, J. Duplissy, M. Gysel, M. Hutterli, J. Kangasluoma, J. Kontkanen, A.Kürten, H. E. Manninen, S. Münch, O. Peräkylä, T. Petäjä, L. Rondo, C. Williamson, E. Weingartner, J.Curtius, D. R. Worsnop, M. Kulmala, J. Dommen, U. Baltensperger, New particle formation in the free troposphere: A question of chemistry and timing. *Science* **352**, 1109-1112 (2016). doi: 10.1126/science.aad5456

13. M. Sipilä , N. Sarnela, T. Jokinen , H. Henschel , H. Junninen , J. Kontkanen , S. Richters , J. Kangasluoma , A. Franchin , O. Peräkylä , M. P. Rissanen , M. Ehn , H. Vehkamäki , T. Kurten, T. Berndt , T. Petäjä , D. R. Worsnop, D. Ceburnis , V.-M. Kerminen , M. Kulmala , C. O'Dowd, Molecular-scale evidence of aerosol particle formation via sequential addition of HIO_3. *Nature* **537**, 532-534 (2016). doi: 10.1038/nature19314

14. M. Kulmala, J. Kontkanen, H. Junninen, K. Lehtipalo, H. E. Manninen, T. Nieminen, T. Petäjä, M. Sipilä, S. Schobesberger, P. Rantala, A. Franchin, T. Jokinen, E. Järvinen, M. Äijälä, J. Kangasluoma, J. Hakala, P. P. Aalto, P. Paasonen, J. Mikkilä, J. Vanhanen, J. Aalto, H. Hakola, U. Makkonen, T. Ruuskanen, R. L. Mauldin 3rd, J. Duplissy, H. Vehkamäki, J. Bäck, A. Kortelainen, I. Riipinen, T. Kurtén, M. V. Johnston, J. N. Smith, M. Ehn, T. F. Mentel, K. E.

Lehtinen, A. Laaksonen, V. -M. Kerminen, D. R. Worsnop, Direct observations of atmospheric aerosol nucleation. *Science* **339**, 943-946 (2013). Medline doi:10.1126/science.1227385.

15. M. Kulmala, V. M. Kerminen, T. Petaja, A. J. Ding, L. Wang, Atmospheric gas-to-particle conversion: why NPF events are observed in megacities. *Faraday Discuss.*, doi:10.1039/C6FD00257A (2017).
16. Z. Wang, Z. Wu, D. Yue, D. Shang, S. Guo, J. Sun, A. Ding, L. Wang, J. Jiang, H. Guo, J. Gao, H. C. Cheung, L. Morawska, M. Keywood, M. Hu, New particle formation in China: Current knowledge and further directions, *Sci. Total Environ.* **577**, 258-266 (2017). doi:10.1016/j.scitotenv.2016.10.177.
17. V. M. Kerminen, M. Kulmala, Analytical formulae connecting the "real" and the "apparent" nucleation rate and the nuclei number concentration for atmospheric nucleation events. *J. Aerosol Sci.* **33**, 609-622 (2002). doi.org/10.1016/S0021-8502(01)00194-X
18. M. Kulmala, V. M. Kerminen, On the formation and growth of atmospheric nanoparticles. *Atmos. Res.* **90**. 132-150 (2008). doi: 10.1016/j.atmosres.2008.01.005
19. M. Kulmala , K. Luoma , A. Virkkula, T. Petäjä, P. Paasonen , V.-M. Kerminen , W. Nie, X. M. Qi, Y.C. Shen, X.G. Chi, A.J. Ding, On the mode-segregated aerosol particle number concentration load: contributions of primary and secondary particles in Hyytiälä and Nanjing. *Boreal Environ. Res.* **21**, 319-331 (2016).
20. Z. Wu, M. Hu, S. Liu, B. Wehner, S. Bauer, A. Ma ßling, A. Wiedensohler, T. Petäjä, M. Dal Maso, M. Kulmala, New particle formation in Beijing, China: Statistical analysis of a 1-year data set. *J. Geophys. Res.-Atmos.* **112**, D09209 (2007). doi: 10.1029/2006JD007406
21. S.Guo, M.Hu, M. L. Zamora, J. F. Peng, D. J. Shang, J. Zheng, Z. F. Du, Z. J. Wu, M. Shao, L.M. Zeng, M.J. Molina, R. Y. Zhang, Elucidating severe urban haze formation in China. *Proc. Natl. Acad. Sci. USA* 111, 17373-17378 (2014). doi:10.1073/pnas.1419604111
22. S. Xiao, M. Y. Wang, L.Yao, M. Kulmala, B. Zhou, X. Yang, J. M. Chen, D. F. Wang, Q. Y. Fu, D. R. Worsnop, L.Wang, Strong atmospheric new particle formation in winter in urban Shanghai, China. *Atmos. Chem. Phys.* **15**, 1769-1781 (2015). doi:10.5194/acp-15-1769-2015
23. X. M. Qi, A. J. Ding, W. Nie, T. Petäjä, V.-M. Kerminen, E. Herrmann, Y. N. Xie, L. F. Zheng, H. Manninen, P. Aalto, J. N. Sun, Z. N. Xu, X. G. Chi, X. Huang, M. Boy, A. Virkkula, X.-Q. Yang, C. B. Fu, M. Kulmala, Aerosol size distribution and new particle formation in the western Yangtze River Delta of China: 2 years of measurements at the SORPES station. *Atmos. Chem. Phys.* **15**, 12445-12464 (2015). doi: 10.5194/acp-15-12445-2015
24. T. Jokinen, M. Sipilä, H. Junninen, M. Ehn, G. Lönn, J. Hakala, T. Petäjä, R. L. Mauldin III, M. Kulmala, D. R. Worsnop, Atmospheric sulphuric acid and neutral cluster measurements using CI-APi-TOF. *Atmos. Chem. Phys.* **12**, 4117-4125 (2012). doi:10.5194/acp-12-4117-2012
25. A. Hamed, H. Korhonen, S.-L. Sihto, J. Joutsensaari, H. Järvinen, T. Petäjä, F. Arnold, T. Nieminen, M. Kulmala, J. N. Smith, K. E. J. Lehtinen, A. Laaksonen, The role of relative humidity in continental new particle formation, *J. Geophys. Res. Atmos.* **116**, D03202 (2011). doi: 10.1029/2010JD014186
26. J. J.Orlando, G. S.Tyndall, Laboratory studies of organic peroxy radical chemistry: an overview with emphasis on recent issues of atmospheric significance, *Chem. Soc. Rev.* **41**, 6294-6317 (2012). doi: 10.1039/c2cs35166h
27. A. Kürten, A. Bergen, M. Heinritzi, M. Leiminger, V. Lorenz, F. Piel, M. Simon, R. Sitals, A. C. Wagner, J. Curtius, Observation of new particle formation and measurement of sulfuric acid,

ammonia, amines and highly oxidized organic molecules at a rural site in central Germany. *Atmos. Chem. Phys.* **16**, 12793-12813 (2016). doi: 10.5194/acp-16-12793-2016

28. T. Petäjä, M. Sipilä, P. Paasonen, T. Nieminen, T. Kurtén, I. K. Ortega, F. Stratmann, H. Vehkamaki, T. Berndt, M. Kulmala, Experimental observation of strongly bound dimers of sulfuric acid: application to nucleation in the atmosphere. *Phys. Rev. Lett.* **106**, 228302-1–228302-4, (2011). doi:10.1103/Physrevlett.106.228302
29. J. Zhao, F. L. Eisele, M. Titcombe, C. G. Kuang, P. H. McMurry, Chemical ionization mass spectrometric measurements of atmospheric neutral clusters using the cluster-CIMS. *J. Geophys. Res.-Atmos.* **115**, D08205 (2010). doi:Artn D0820510.1029/2009jd012606
30. F. Bianchi, A. P. Praplan, N. Sarnela, J. Dommen, A. Kürten, I. K. Ortega, S. Schobesberger, H. Junninen, M. Simon, J. Tröstl, T. Jokinen, M. Sipilä, A. Adamov, A. Amorim, J. Almeida, M. Breitenlechner, J. Duplissy, S. Ehrhart, R. C. Flagan, A. Franchin, J. Hakala, A. Hansel, M. Heinritzi, J. Kangasluoma, H. Keskinen, J. Kim, J. Kirkby, A. Laaksonen, M. J. Lawler, K. Lehtipalo, M. Leiminger, V. Makhmutov, S. Mathot, A. Onnela, T. Petäjä, F. Riccobono, M. P. Rissanen, L. Rondo, A. Tomé, A. Virtanen, Y. Viisanen, C. Williamson, D. Wimmer, P. M. Winkler, P. Ye, J. Curtius, M. Kulmala, D. R. Worsnop, N. M. Donahue, U. Baltensperger, Insight into acid-base nucleation experiments by comparison of the chemical composition of positive, negative, and neutral clusters. *Environ. Sci. Technol.* **48**, 13675-13684 (2014). Medline doi:10.1021/es502380b
31. M. Ehn, J. A. Thornton, E. Kleist, M. Sipilä, H. Junninen, I. Pullinen, M. Springer, F. Rubach, R. Tillmann, B. Lee, F. Lopez-Hilfiker, S. Andres, I.-H. Acir, M. Rissanen, T. Jokinen, S. Schobesberger, J. Kangasluoma, J. Kontkanen, T. Nieminen, T. Kurtén, L. B. Nielsen, S. Jørgensen, H. G. Kjaergaard, M. Canagaratna, M. D. Maso, T. Berndt, T. Petäjä, A. Wahner, V.-M. Kerminen, M. Kulmala, D. R. Worsnop, J. Wildt, T. F. Mentel, A large source of low-volatility secondary organic aerosol. *Nature* **506**, 476-479 (2014). Medline doi:10.1038/nature13032
32. P. Paasonen, T. Olenius, O. Kupiainen, T. Kurtén, T. Petäjä, W. Birmili, A. Hamed, M. Hu, L. G. Huey, C. Plass-Duelmer, J. N. Smith, A. Wiedensohler, V. Loukonen, M. J. McGrath, I. K. Ortega1, A. Laaksonen, H. Vehkamäki, V.-M. Kerminen, M. Kulmala, On the formation of sulphuric acid - amine clusters in varying atmospheric conditions and its influence on atmospheric new particle formation. *Atmos. Chem. Phys.* **12**, 9113-9133 (2012). doi: 10.5194/acp-12-9113-2012
33. L. Yao , M. Y. Wang , X. K. Wang , Y. J. Liu , H. F. Chen , J. Zheng , W. Nie, A.J. Ding , F. H. Geng , D. F. Wang , J. M. Chen , D. R. Worsnop , L. Wang, Detection of atmospheric gaseous amines and amides by a high-resolution time-of-flight chemical ionization mass spectrometer with protonated ethanol reagent ions. *Atmos. Chem. Phys.* **16**, 14527-14543 (2016). doi: 10.5194/acp-16-14527-2016
34. K. Lehtipalo, L. Rondo, J. Kontkanen, S. Schobesberger, T. Jokinen, N. Sarnela, A. Kürten, S. Ehrhart, A. Franchin, T. Nieminen, F. Riccobono, M. Sipilä, T. Yli-Juuti, J. Duplissy, A. Adamov, L. Ahlm, J. Almeida, A. Amorim, F. Bianchi, M. Breitenlechner, J. Dommen, A. J. Downard, E. M. Dunne, R. C. Flagan, R. Guida, J. Hakala, A. Hansel, W. Jud, J. Kangasluoma, V.-M. Kerminen, H. Keskinen, J. Kim, J. Kirkby, A. Kupc, O. Kupiainen-Määttä, A. Laaksonen, M. J. Lawler, M. Leiminger, S. Mathot, T. Olenius, I. K. Ortega, A. Onnela, T. Petäjä, A. Praplan, M. P. Rissanen, T. Ruuskanen, F. D. Santos, S. Schallhart, R. Schnitzhofer, M. Simon, J. N. Smith,

J. Tröstl, G. Tsagkogeorgas, A. Tomé, P. Vaattovaara, H. Vehkamäki, A. E. Vrtala, P. E. Wagner, C. Williamson, D. Wimmer, P. M. Winkler, A. Virtanen, N. M. Donahue, K. S. Carslaw, U. Baltensperger, I. Riipinen, J. Curtius, D. R. Worsnop, M. Kulmala, The effect of acid-base clustering and ions on the growth of atmospheric nano-particles. *Nat. Commun.* **7**, 11594 (2016). doi: 10.1038/ncomms11594

35. J. Tröstl, W. K. Chuang, H. Gordon, M. Heinritzi, C. Yan, U. Molteni, L. Ahlm, C. Frege, F. Bianchi, R. Wagner, M. Simon, K. Lehtipalo, C. Williamson, J. S. Craven, J. Duplissy, A. Adamov, J. Almeida, A.-K. Bernhammer, M. Breitenlechner, S. Brilke, A. Dias, S. Ehrhart, R. C. Flagan, A. Franchin, C. Fuchs, R. Guida, M. Gysel, A. Hansel, C. R. Hoyle, T. Jokinen, H. Junninen, J. Kangasluoma, H. Keskinen, J. Kim, M. Krapf, A. Kürten, A. Laaksonen, M. Lawler, M. Leiminger, S. Mathot, O. Möhler, T. Nieminen, A. Onnela, T. Petäjä, F. M. Piel, P. Miettinen, M. P. Rissanen, L. Rondo, N. Sarnela, S. Schobesberger, K. Sengupta, M. Sipilä, J. N. Smith, G. Steiner, A. Tomè, A. Virtanen, A. C. Wagner, E. Weingartner, D. Wimmer, P. M. Winkler, P. Ye, K. S. Carslaw, J. Curtius, J. Dommen, J. Kirkby, M. Kulmala, I. Riipinen, D. R. Worsnop, N. M. Donahue, U. Baltensperger, The role of low-volatility organic compounds in initial particle growth in the atmosphere. *Nature* **533**, 527-531 (2016). doi:10.1038/nature18271

36. P. Paasonen, K. Kupiainen, Z. Klimont, A. Visschedijk, H. A. C. Denier van der Gon, M. Amann, Continental anthropogenic primary particle number emissions. *Atmos. Chem. Phys.* **16**, 6823-6840 (2016). doi: 10.5194/acp-16-6823-2016

37. C. Huang, C. H. Chen, L. Li, Z. Cheng, H. L. Wang, H. Y. Huang, D. G. Streets, Y. J. Wang, G. F. Zhang, Y. R. Chen, Emission inventory of anthropogenic air pollutants and VOC species in the Yangtze River Delta region, China. *Atmos. Chem. Phys.* **11**, 4105-4120 (2011). doi: 10.5194/acp-11-4105-2011

38. J. Zheng, Y. Ma, M. D. Chen, Q. Zhang, L. Wang, A. F. Khalizov, L. Yao, Z. Wang, X. Wang, L.X. Chen, Measurement of atmospheric amines and ammonia using the high resolution time-of-flight chemical ionization mass spectrometry. *Atmos. Environ.* **102**, 249-259 (2015). doi: 10.1016/j.atmosenv.2014.12.002

39. Y. Ma, X. Xu, W. H. Song, F. Geng, L. Wang, Seasonal and diurnal variations of particulate organosulfates in urban Shanghai, China. *Atmos. Environ.* **85**, 152-160 (2014). doi: 10.1016/j.atmosenv.2013.12.017

40. L. Wang, H. Du, J. M. Chen, M. Zhang, X. Huang, H. Tan, L. Kong, F. Geng, Consecutive transport of anthropogenic air masses and dust storm plume: Two case events at Shanghai, China. *Atmos. Res.* **127**, 22-33 (2013). doi:10.1016/j.atmosres.2013.02.011

41. X. K. Wang, S. Rossignol, Y. Ma, L. Yao, M. Y. Wang, J. M. Chen, C. George, L. Wang, Molecular characterization of atmospheric particulate organosulfates in three megacities at the middle and lower reaches of the Yangtze River. *Atmos. Chem. Phys.* **16**, 2285-2298 (2016). doi:10.5194/acp-16-2285-2016

42. J. Vanhanen, J. Mikkilä, K. Lehtipalo, M. Sipilä, H. E. Manninen, E. Siivola, T. Petäjä, M. Kulmala, Particle size magnifier for nano-CN detection. *Aerosol Sci. Technol.* **45**, 533-542 (2011). doi:10.1080/02786826.2010.547889

43. K. Lehtipalo, J. Leppä, J. Kontkanen, J. Kangasluoma, A. Franchin, D. Wimmer, S. Schobesberger, H. Junninen, T. Petäjä, M. Sipilä, J.Mikkilä, J. Vanhanen, D. R. Worsnop, M. Kulmala, Methods for determining particle size distribution and growth rates between 1 and 3 nm using the Particle Size Magnifier. *Boreal Environ. Res.* **19**, 215-236 (2014).

44. S. Mirme, A. Mirme, The mathematical principles and design of the NAIS - a spectrometer for the measurement of cluster ion and nanometer aerosol size distributions. *Atmos. Meas. Tech.* **6**, 1061-1071 (2013). doi:10.5194/amt-6-1061-2013

45. H. E. Manninen, S. Mirme, A. Mirme, T. Petäjä, M. Kulmala, How to reliably detect molecular clusters and nucleation mode particles with Neutral cluster and Air Ion Spectrometer (NAIS). *Atmos. Meas. Tech.* **9**, 3577-3605 (2016). doi:10.5194/amt- 9-3577-2016

46. H. E. Manninen, A. Franchin, S. Schobesberger, A. Hirsikko, J. Hakala, A. Skromulis, J. Kangasluoma, M. Ehn, H. Junninen, A. Mirme, S. Mirme, M. Sipilä, T. Petäjä, D. R. Worsnop, M. Kulmala, Characterisation of corona-generated ions used in a Neutral cluster and Air Ion Spectrometer (NAIS). *Atmos. Meas. Tech.* **4**, 2767-2776 (2011). doi:10.5194/amt-4-2767-2011

47. R.Wagner, H. E. Manninen , A. Franchin , K. Lehtipalo, S. Mirme, G. Steiner, T. Petäjä, M. Kulmala, On the accuracy of ion measurements using a Neutral cluster and Air Ion Spectrometer. *Boreal Environ. Res.* **21**, 230-241 (2016).

48. H. Junninen, M. Ehn, T. Petäjä, L. Luosujärvi, T. Kotiaho, R. Kostiainen , U. Rohner, M. Gonin , K. Fuhrer, M. Kulmala, D. R. Worsnop, A high-resolution mass spectrometer to measure atmospheric ion composition. *Atmos. Meas. Tech.* **3**, 1039-1053 (2010). doi:10.5194/amt-3-1039-2010

49. F. L. Eisele, D. Tanner, Measurement of the gas-phase concentration of H_2SO_4 and methane sulfonic-acid and estimates of H_2SO_4 production and loss in the atmosphere. *J Geophys Res-Atmos* **98**, 9001-9010 (1993). doi:10.1029/93JD00031

50. T. H. Bertram, J. R. Kimmel, T. A. Crisp, O. S. Ryder, R. L. N. Yatavelli, J. A. Thornton, M. J. Cubison, M. Gonin, D. R. Worsnop, A field-deployable, chemical ionization time-of-flight mass spectrometer. *Atmos. Meas. Tech.* **4**, 1471-1479 (2011). doi:10.5194/amt-4-1471-2011

51. J. Zheng, D. S. Yang, Y. Ma, M. D. Chen, J. Cheng, S.Z. Li, M. Wang. Development of a new corona discharge based ion source for high resolution time-of-flight chemical ionization mass spectrometer to measure gaseous H_2SO_4 and aerosol sulfate. *Atmos. Environ.* **119**, 167-173, (2015). doi: 10.1016/j.atmosenv.2015.08.028

52. S. Mikkonen, S. Romakkaniemi, J. N. Smith, H. Korhonen, T. Petäjä, C. Plass-Duelmer, M. Boy, P. H. McMurry, K. E. J. Lehtinen, J. Joutsensaari, A. Hamed, R. L. Mauldin III, W. Birmili, G. Spindler, F. Arnold, M. Kulmala, A. Laaksonen, A statistical proxy for sulphuric acid concentration. *Atmos. Chem. Phys.* **11**, 11319-11334 (2011). doi: 10.5194/acp-11-11319-2011

53. D. R. Hanson, F. L. Eisele, Measurement of prenucleation molecular clusters in the NH_3, H_2SO_4, H_2O system. *J Geophys Res-Atmos* **107**, AAC 10-1- AAC 10-18 (2002). doi: 10.1029/2001JD001100

54. M. J. McGrath, T. Olenius, I. K. Ortega, V. Loukonen, P. Paasonen, T. Kurtén, M. Kulmala, H. Vehkamäki, Atmospheric Cluster Dynamics Code: a flexible method for solution of the birth-death equations, *Atmos. Chem. Phys.* **12**, 2345-2355 (2012). doi: 10.5194/acp-12-2345-2012

55. M. Kulmala, T. Petäjä, T. Nieminen, M. Sipilä, H. E. Manninen, K. Lehtipalo, M. Dal Maso, P. P. Aalto, H. Junninen, P. Paasonen, I. Riipinen, K. E. Lehtinen, A. Laaksonen, V. M. Kerminen, Measurement of the nucleation of atmospheric aerosol particles. *Nat. protoc.* **7**, 1651-1667 (2012). Medline doi:10.1038/nprot.2012.091

56. K. E. J. Lehtinen, M. Dal Maso, M. Kulmala, V. -M. Kerminen, Estimating nucleation rates from apparent particle formation rates and vice versa: Revised formulation of the Kerminen-Kulmala equation. *J .Aerosol. Sci.* **38**, 988-994 (2007). doi: 10.1016/j.jaerosci.2007.06.009

57. T. Yli-Juuti, T. Nieminen, A. Hirsikko, P. P. Aalto, E. Asmi, U. Hõrrak, H. E. Manninen, J. Patokoski, M. Dal Maso, T. Petäjä, J. Rinne, M. Kulmala, I. Riipinen, Growth rates of nucleation mode particles in Hyytiala during 2003-2009: variation with particle size, season, data analysis method and ambient conditions. *Atmos. Chem. Phys.* **11**, 12865-12886 (2011). doi:10.5194/acp-11-12865-2011

58. T. Nieminen, K. E. J. Lehtinen, M. Kulmala, Sub-10 nm particle growth by vapor condensation - effects of vapor molecule size and particle thermal speed. *Atmos. Chem. Phys.* **10**, 9773-9779 (2010). doi:10.5194/acp-10-9773-2010

59. M. Amanna, I.Bertoka , J. Borken-Kleefelda , J. Cofalaa , C. Heyesa , L. Höglund-Isakssona , Z. Klimonta , B. Nguyena , M. Poschb , P. Rafaja , R. Sandlera , W. Schöppa , F. Wagnera , W. Winiwarter, Cost-effective control of air quality and greenhouse gases in Europe: Modeling and policy applications. *Environ. Modell. Softw.* **26**, 1489-1501, (2011). doi: 10.1016/j.envsoft.2011.07.012

Acknowledgements

This study was financially supported by the National Natural Science Foundation of China (No. 21190053, 21222703, 21561130150, & 91644213), the Ministry of Science and Technology of China (2017YFC0209505), the Cyrus Tang Foundation (No. CTF-FD2014001), the Academy of Finland Centre of Excellence program (project no 272041, 307331), European Research Council (COALA, grant 638703), European Research Council (GASPARCON, grant 714621), Swiss National Science Foundation (grant P2EZP2_168787), and Academy of Finland (Project no. 296628 and 306853). These results are part of a project (ATM-GTP /ERC) that has received funding from the European Research Council (ERC) under the European Union's Horizon 2020 research and innovation program (grant agreement No 742206). L.W. thanks the Royal Society-Newton Advanced Fellowship (NA140106). M.K. acknowledges the support by the Academy of Finland via his Academy Professorship (no. 302958). Katrianne Lehtipalo, Lauri Ahonen and Dominik Stolzenburg are acknowledged for useful discussions. We also thank the tofTools team for providing tools for mass spectrometry analysis. All data related to this study can be obtained from the corresponding author (Lin Wang) via email: lin_wang@fudan.edu.cn.

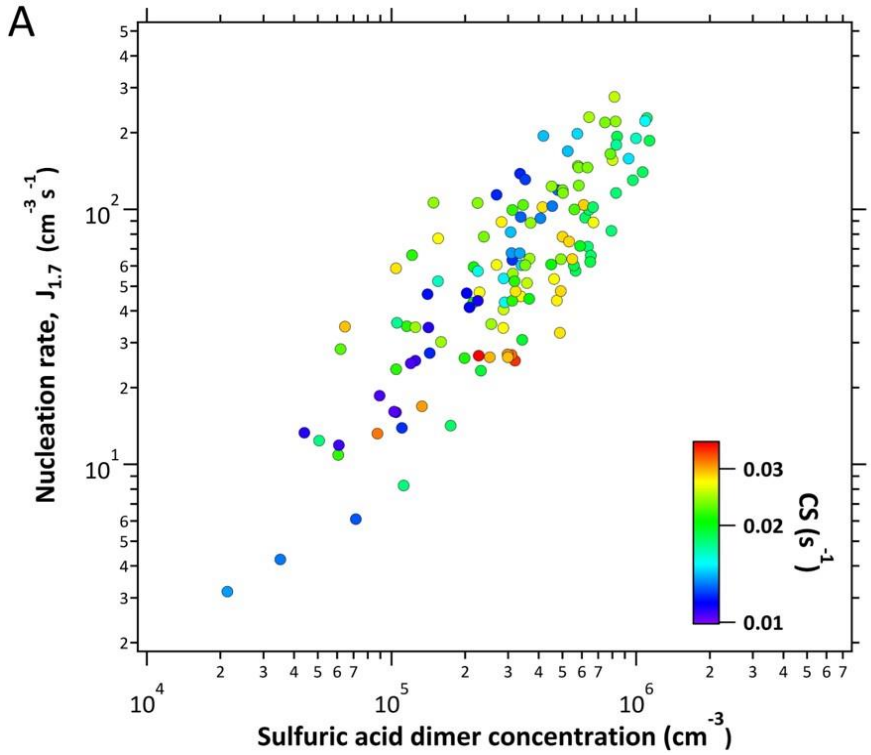
A
Nucleation rate, $J_{1.7}$ (cm^{-3} s^{-1})
Sulfuric acid dimer concentration (cm^{-3})
CS (s^{-1})
0.03
0.02
0.01

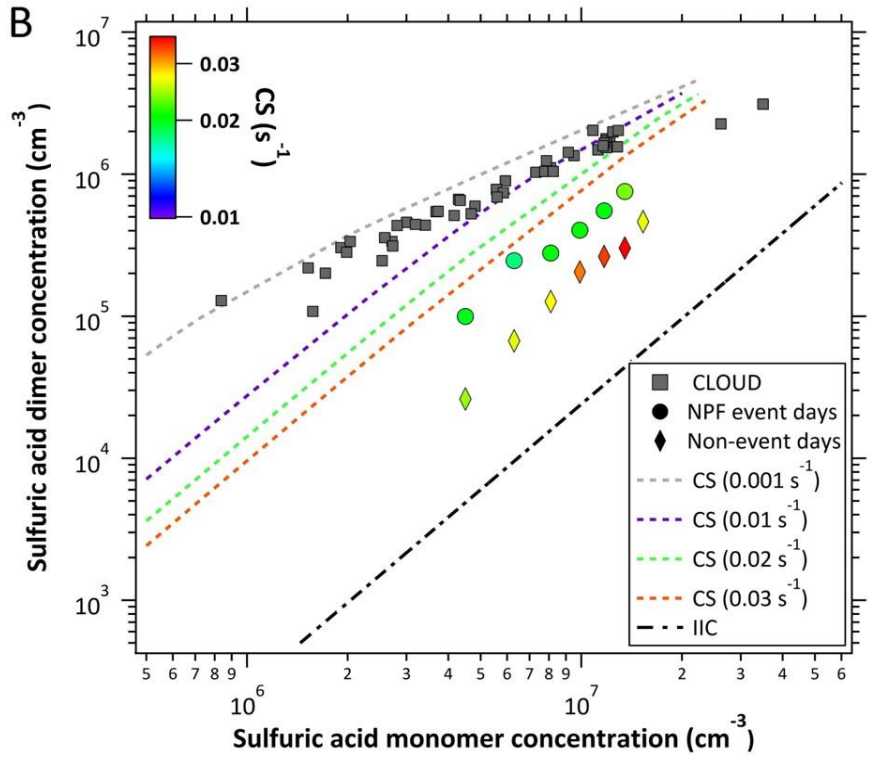
B
Sulfuric acid dimer concentration (cm^{-3})
Sulfuric acid monomer concentration (cm^{-3})
CS (s^{-1})
0.03
0.02
0.01
CLOUD
NPF event days
Non-event days
CS (0.001 s^{-1})
CS (0.01 s^{-1})
CS (0.02 s^{-1})
CS (0.03 s^{-1})
IIC

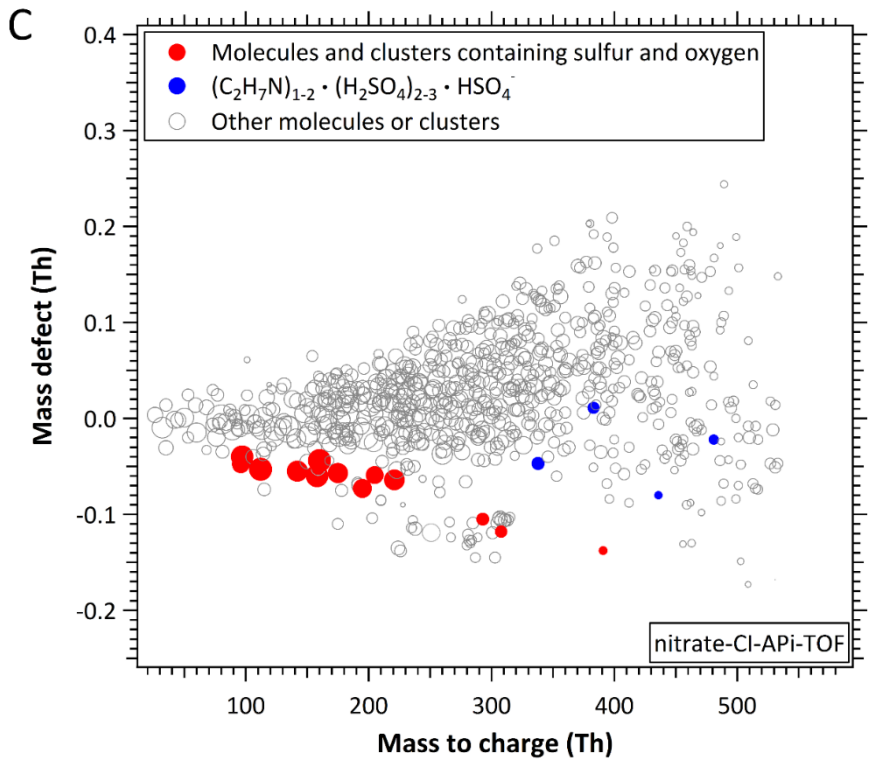

Fig.1. Sulfuric acid clusters (dimer, trimer, and tetramer), sulfuric acid-DMA clusters and particle formation rates. (**A**) Particle formation rates ($J_{1.7}$) as a function of sulfuric acid concentration. The color-coding denotes different CS values. (**B**) Sulfuric acid dimer concentration as a function of sulfuric acid monomer concentration. Grey squares correspond to experimental observations of H_2SO_4-DMA-H_2O nucleation in the CLOUD experiment (*6,9*). The colored dashed lines show the sulfuric acid dimer concentration from cluster kinetics simulations under different CS. The dashed-dotted line shows the theoretical maximum of sulfuric acid dimer concentration from an ion-induced clustering (IIC) of neutral sulfuric acid and bisulfate ions within the CI-APi-TOF ion reaction zone (*29*). The data for the whole intensive campaign was separated into NPF and non-event days. The sulfuric acid monomer concentration was divided into linear bins and the median values of sulfuric acid dimer concentration in each bin is shown as circles (NPF event days) and diamonds (non-event days). (**C**) CI-APi-TOF mass defect plot during a new particle formation event (11:00-13:00, 6 February 2016, local time, CS=0.019 s^{-1}). Presented are compounds containing sulfur and oxygen (red circles) (table S2), sulfuric acid-dimethylamine clusters (blue circles), and other molecules or clusters (open circles). The symbol size is proportional to the logarithm of the signal intensity (count rate). The sulfuric acid concentration, relative humidity, and temperature during the nucleation period were 1.1×10^7 cm^{-3}, 37%, and 280 K, respectively. High-resolution peak fitting to CI-APi-TOF data for all 9 NPF events is shown in fig. S5.

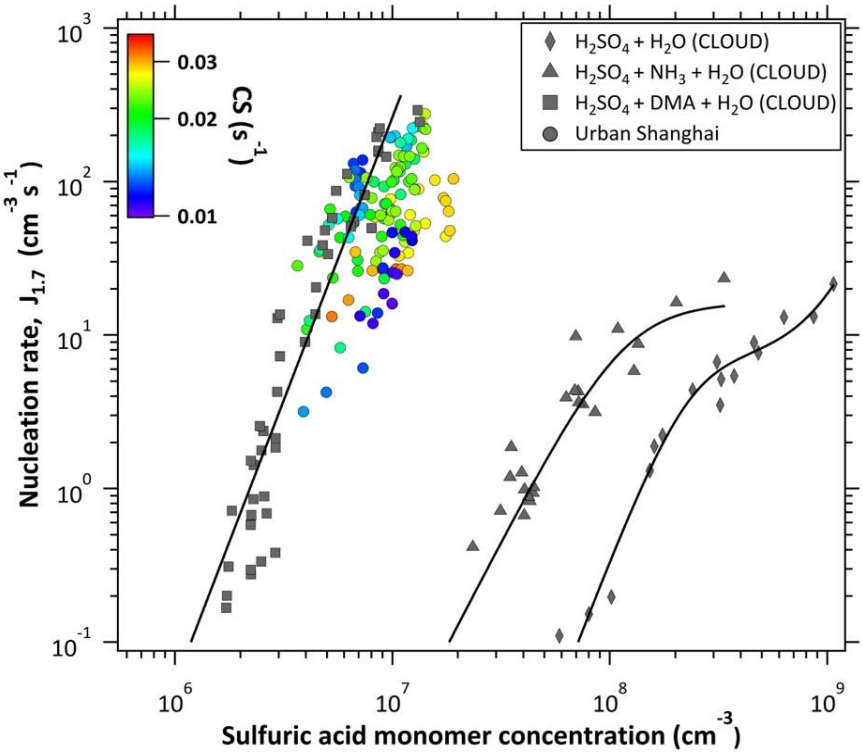

Fig. 2. Comparison of ambient and CLOUD particle formation rates against sulfuric acid monomer concentration. Grey diamonds, triangles, and squares denote CLOUD data for H_2SO_4-H_2O, H_2SO_4-NH_3-H_2O, and H_2SO_4-DMA-H_2O nucleation, respectively, at 38% RH and 278K (*9,10*). The color-coding denotes different CS values. The lines are plotted to guide the eye.

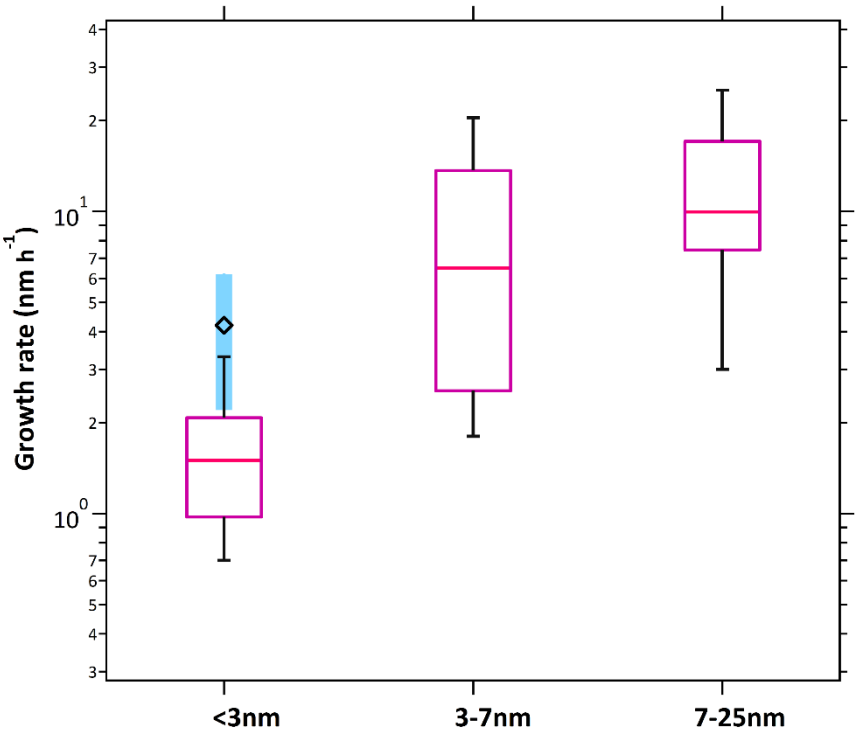

Fig. 3. Particle growth rates during NPF events. Growth rate (GR) in different size ranges (< 3 nm, 3-7 nm, and 7-25 nm) during the intensive campaign. $GR_{<3nm}$ was determined from PSM measurements, whereas $GR_{\geq 3nm}$ was calculated using nano-SMPS data. The pink horizontal lines show the median GR, purple boxes show the 25th and 75th percentile values, and whiskers 10th and 90th percentile values. The black diamond shows $GR_{<3nm}$ from cluster kinetics simulations for a collision-limited H_2SO_4-DMA system with median sulfuric acid concentration and CS for the NPF events (1.3×10^{7} cm^{-3} and 2.1×10^{-2} s^{-1}). The blue box shows simulation results assuming 50% higher or lower sulfuric acid concentration due to the uncertainty in measured H_2SO_4.

Supplementary Materials:

Materials and Methods

Figures S1-S16

Tables S1-S2

References and notes (39-59)

Author Information: The authors declare no competing financial interests. Correspondence and requests for materials should be addressed to Lin Wang (lin_wang@fudan.edu.cn).

Supplementary Materials for

Atmospheric New Particle Formation from Sulfuric Acid and Amines in a Chinese Megacity

Lei Yao, Olga Garmash, Federico Bianchi, Jun Zheng, Chao Yan, Jenni Kontkanen, Heikki Junninen, Stephany Buenrostro Mazon, Mikael Ehn, Pauli Paasonen, Mikko Sipilä, Mingyi Wang, Xinke Wang, Shan Xiao, Hangfei Chen, Yiqun Lu, Bowen Zhang, Dongfang Wang, Qingyan Fu, Fuhai Geng, Li Li, Hongli Wang, Liping Qiao, Xin Yang, Jianmin Chen, Veli-Matti Kerminen, Tuukka Petäjä, Douglas R.Worsnop, Markku Kulmala, Lin Wang

correspondence to: lin_wang@fudan.edu.cn

This PDF file includes:

Material and Methods

Introduction of the sampling site

Located in the campus of Fudan University, the Fudan monitoring site (31° 17′ 54" N, 121° 30′ 05" E) is on the rooftop of a teaching building that is ~ 20 m above ground (Fig. S1). About 100 m to the north is the "Middle Ring", which is one of the main overhead highways in Shanghai. This site is also influenced by local industrial and residential activities. Therefore, the Fudan monitoring site is a representative of an urban site (*22,33,39-41*).

Most measurements were conducted at the Fudan site. Using a high flow rate blower, ambient air was drawn into a stainless-steel manifold of 5 m length and 4 inch inner diameter at a flow rate of 4 cubic meters per minute (m^3 min^{-1}). The tubing between the main manifold and the instruments was kept as short as possible to reduce wall loss of small particles.

Concentrations of trace gases (NO_x, SO_2, O_3 and CO) and meteorological parameters, including temperature, relative humidity (RH), wind speed and direction as well as precipitation, were recorded at the Yangpu Sipiao monitoring site (31°15′58″ N, 121°32′1″ E, about 5.1 km from the Fudan site) of Shanghai environmental monitoring center. Solar radiation intensities were obtained from Shanghai Pudong environmental monitoring center (31°13′44″ N, 121°32′2″ E, about 8.8 km from the Fudan site).

Aerosol properties - number size distribution

The Particle Size Magnifier (PSM)

Number size distributions of sub-3 nm clusters/particles were measured from March 2014 to February 2016 using an Airmodus A10 particle size magnifier (PSM) coupled with an Airmodus A20 condensation particle counter (CPC) (*42*). Diethylene glycol was used as a working fluid of PSM, allowing clusters/particles to grow up to ~90 nm in diameter by condensation of diethylene glycol vapour inside PSM. Particles were then directed into the A20 CPC to further grow to optically detectable sizes by condensation of *n*-butanol vapour. The cut-off sizes of PSM can be varied by altering the mixing ratios of the sample and the saturator flows. PSM was operated in a 120-step scanning mode with the saturator flow rate between 0.1 and 1.0 L min^{-1}. The time resolution of a full scan was 240 s. The ambient sample was diluted by pure air with a dilution ratio of 1:2 to minimize the influences of ambient relative humidity and aerosol loading on the saturation of diethylene glycol in PSM. Gaussian-shaped kernel functions were used for the data inversion (*43*). The raw data were inverted into particle numbers in five size bins of 1.2-1.5 nm, 1.5-1.7 nm, 1.7-2.0 nm, 2.0-2.7 nm, and 2.7-3 nm.

The Neutral cluster and Air Ion Spectrometer (NAIS)

NAIS (Airel Ltd., Estonia) was deployed during the intensive campaign (December 2015 to February 2016). It is an ion mobility spectrometer that measures the number size distribution of ions and total particles with electrical mobilities from 3.2 to 0.0013 $cm^2\ V^{-1}\ s^{-1}$ (*44,45*), which is equivalent to Milikan mobility diameters of 0.8 to 42 nm.

NAIS comprises two differential mobility analyzers to measure in parallel both negative and positive polarities using 21 electrometers, respectively. The measurement cycle of NAIS includes 1) an ion mode (ions and naturally charged aerosols), 2) a total particle mode (ions and neutral particles), and 3) an offset mode to detect the electrometer noise levels. The full measurement cycle lasts ~3 min. During the total particle mode, neutral aerosols are charged inside the instrument with a corona charger needle. The diameters of the resulting corona ions have been measured to be around 1-1.6 nm (*46*). Since they are not part of the ambient aerosol population, concentrations of total particles in this size range should be discarded from analysis. The standard NAIS high sample flow rate of 54 L min^{-1} (27 L min^{-1} per polarity) and sheath flow of 60 L min^{-1} were used.

Prior to data analysis, a transmission correction was applied to the raw NAIS data, using the function $f(d_p) = a(d_p)^b$, where d_p is the mobility diameter in nm, a= 0.713, and b= 0.120 (see Table 2 in the Wagner *et al.* study (*47*)). No external inlet tube was added to the instrument, and no additional inlet transmission corrections were applied.

The Scanning Mobility Particle Sizer (SMPS)

Two SMPSs (nano- and long-SMPS, TSI Inc, USA) were deployed to measure number size distributions of 3-736 nm particles for two years (March 2014 to February 2016). A nano-SMPS, consisting of a nano-differential mobility analyzer and a condensation particle counter (CPC) 3776, measured aerosol size distribution from 3 nm to 65 nm in mobility diameter. A long-SMPS, consisting of a long-differential mobility analyzer and a CPC 3775, covered the particle size distribution from 14 nm to 736 nm. The time resolution for SMPS data acquisition was 5 min.

A neutralizer (Kr-85) was used to neutralize electrostatic charges on aerosol particles. The SMPS data were corrected for single charging efficiency, multiple charges, and diffusion losses.

Molecule and cluster composition

The APi-TOF mass spectrometer

The Atmospheric Pressure interface time-of-flight (APi-TOF) mass spectrometer (*48*) (Tofwerk AG, Switzerland and Aerodyne Research Inc, USA) was deployed to measure the mass-to-charge ratio (*m/z*) of ambient natural ions (positive or negative) with an inlet operated at the atmospheric pressure. Once the ions entered the APi-TOF, they

were guided by segmented quadrupole mass filters and an ion lens. The pressures of the Small-Segmented Quadrupole (SSQ), Big-Segmented Quadrupole (BSQ), and Time-of-Flight (TOF) region were regulated at ~ 2.5, ~ 3.6×10^{-2} and ~ 1.1×10^{-6} mbar, respectively. Operating in V-mode, the mass resolving power is around 4500 Th/Th (Th, Thomson) and the mass accuracy is better than 10 ppm.

A stainless-steel tube with an inner diameter of 1 inch and a length of 0.6 m was used as the sampling tube, and the flow rate was 50 L min^{-1}. A home-made flange adapter was used to connect the stainless-steel sampling tube and APi part. The sample flow rate into APi-TOF was 0.8 L min^{-1} and was controlled by a 300 μm orifice.

The CI-APi-TOF mass spectrometer

A nitrate-based Chemical Ionization - Atmospheric Pressure interface - Time-of-Flight (CI-APi-TOF, Aerodyne Research Inc, USA and Tofwerk AG, Switzerland) mass spectrometer was utilized to detect neutral gas-phase sulfuric acid (SA), highly oxidized molecules (HOMs), and other clusters (*6,24,31*). The CI-APi-TOF consists of an optimized inlet for chemical ionization (CI-inlet) (*49*) and an APi-TOF mass spectrometer (*48*).

In the charging region of CI-inlet, the sample flow stays in the center and is surrounded by a sheath air carrying the nitrate ions that are electrostatically pushed into the sample flow. The sheath and sample flow rates were 20 L min^{-1} and 10 L min^{-1}, respectively. Under such condition, the ion-molecule reaction time in the CI-inlet was ~200 ms. Pure air (relative humidity < 5 %) generated from a pure air generator (Aadco 737) was adopted as the sheath air to reduce the production of water-nitrate clusters. In addition, the SO_2 mixing ratio in sheath flow was less than 0.02 ppbv (parts per billion by volume). Hence, the influence of sulfuric acid derived from the oxidation of SO_2 in the sheath flow was minor. Ambient air was drawn into the CI-inlet through a ¾ inch stainless steel tube with a length of 0.47 m. A flow of 0.8 L min^{-1} from the mixed flow passed through a critical orifice with a diameter of 300 μm to enter the APi-TOF. The mass spectrometer was operated in the negative V-mode with a mass resolution of ~ 4800 Th/Th at *m/z* 188 and a mass accuracy better than 10 ppm. Data of CI-APi-TOF were acquired at 1 Hz time resolution and analyzed with a MATLAB tofTools package (*48*), Tofware (Aerodyne Research, Inc. and Tofwerk AG), and Igor Pro (Wavemetrics).

For high *m/z* calibration, a flow with a low concentration of C_5-perfluorinated acid (C_4F_9COOH) generated from a self-made permeation source was directed into CI-APi-TOF as standards. In nitrate-based CI-APi-TOF, C_5-perfluorinated acid can be detected as deprotonated C_5-perfluorinated acid ($C_4F_9COO^-$, *m/z* 262.9760), monomer clustered with nitrate ions ($C_4F_9COOH\cdot NO_3^-$, *m/z* 325.9716), and dimer ($C_4F_9COOH\cdot C_4F_9COO^-$, *m/z* 526.9593).

The ethanol HR-ToF-CIMS

An Aerodyne high-resolution time-of-flight chemical ionization mass spectrometer (HR-ToF-CIMS) (*50*) with protonated ethanol reagent ions was deployed to detect

gaseous C_2-amines (most likely dimethylamine, DMA) in August 2015 (*33*). For the purpose of detection of amines, the CI-inlet was replaced by an ion-molecule reaction (IMR) chamber regulated at ~100 mbar. The sample flow (1.35 L min^{-1}) and the reagent ion flow (1 L min^{-1}) converged in IMR where the ion-molecule reaction occurred between protonated ethanol ions and C_2-amines. The ion-molecule reactions of C_2-amines (denoted as A) with protonated ethanol reagent ions can be represented by the following reaction (*33*):

$$(C_2H_5OH)_n \cdot H^+ + A \longrightarrow (C_2H_5OH)_j \cdot A \cdot H^+ + (n\text{-}j)\ C_2H_5OH \quad (R1)$$

where n = 1, 2, and 3, and j = 0 and 1.

Fig. S7 shows the plot for the particle concentration in the smallest size bin (1.2-1.5 nm) of PSM versus [(C_2-amines×sulfuric acid)/(condensation sink, *i.e.*, CS)], [C_2-amine]/CS, and calculated [SA]/CS, respectively, on 12th August 2015. The results clearly indicate that sulfuric acid was the driving force for NPF, and also that NPF is derived from the synergistic effect of SA and DMA. Statistical comparison of DMA concentrations (between July 2015 and August 2015) between event and non-event days (Fig. S8) also hints the important roles of C_2-amines in new particle formation.

Determination of sulfuric acid and HOMs

Nitrate ions were used as reagent ions to charge analytes via collisions. In the CI-inlet, the sheath gas carrying a small amount of nitric acid (HNO_3) vapour was exposed to an X-ray source (Hamamatsu L9491) to generate the reagent ions ($NO_3^-\cdot(HNO_3)_{n=0\text{-}2}$). The ion-molecule reactions of sulfuric acid and HOMs with nitrate reagent ions can be described by the following reactions:

$$H_2SO_4 + NO_3^-\cdot(HNO_3)_n \longrightarrow HSO_4^-\cdot(HNO_3)_j + (n\text{-}j+1)\ HNO_3 \quad (R2)$$

$$HOM + NO_3^-\cdot(HNO_3)_n \longrightarrow HOM\cdot NO_3^- + n\ HNO_3 \quad (R3)$$

where n=0, 1 or 2 and j=0 or 1. Because sulfuric acid is a stronger acid, de-protonation takes place during its collision with nitrate ions. Therefore, sulfuric acid can be detected as de-protonated monomer ions and cluster ions with HNO_3. Nonetheless, unlike sulfuric acid, most HOMs are detected as adducts with NO_3^-.

To take the variation in the total reagent ions into account, neutral sulfuric acid was quantified according to:

$$[H_2SO_4] = \mathrm{C} \times \frac{\sum_{n=0-1}(HSO_4^-) \cdot (HNO_3)_n}{\sum_{n=0-2}(NO_3^-) \cdot (HNO_3)_n} \quad E(1)$$

where C (in units of cm^{-3}) is a calibration coefficient obtained through an inter-comparison with another calibrated aerodyne high-resolution time-of-flight chemical ionization mass spectrometer (HR-ToF-CIMS) sampling at the same location. The second HR-ToF-CIMS was calibrated by in-situ generated H_2SO_4 (*51*). The calibration coefficient C was determined as 6.0×10^9 cm^{-3} (Fig. S13). Assuming an identical sampling line loss, transmission efficiency, and charging efficiency for sulfuric acid

monomers and dimers, we quantified sulfuric acid dimers using the calibration coefficient of monomers. Since the transmission efficiency and charging efficiency of SA-DMA clusters were likely different from those of SA monomer, this calibration factor was not used to quantify SA-DMA clusters. Total organic concentration from CI-APi-TOF was calculated similarly to the equation E(1), but in numerator, sum of signal for individual HOMs was used (ΣHOM). The uncertainty of the absolute sulfuric acid monomer, sulfuric acid dimer and HOM concentrations was taken as ±50% (*31*). At the same time, relative changes in concentration in time as well as among the detected species were captured by CI-APi-TOF with <10% precision (*31*). No direct calibration for HOMs was conducted.

For the long-term observation without mass spectrometric measurements, sulfuric acid concentration was calculated using a proxy method (*27,52*):

$$[H_2SO_4]_{proxy} = a \times k\ (\mathrm{T},\ \mathrm{p}) \times [\mathrm{SO_2}]^b \times \mathrm{Rad}^c \times \mathrm{RH}^d \times \mathrm{CS}^e \qquad E(2)$$

where k is a rate constant depending on ambient temperature T and pressure p, $[SO_2]$ is the mixing ratio (in ppbv), Rad is the radiation (in W m^{-2}), RH is the relative humidity (%), CS is condensation sink (in s^{-1}), and the coefficients $a = 1.321 \times 10^{15}$, $b = 0.913$, $c = 0.990$, $d = -0.217$ and $e = -0.526$ (*27*).

In order to improve the reliability of this proxy method, a comparison of calculated and measured sulfuric acid was conducted for data between 09:00 and 14:00 on the NPF days during the intensive campaign, yielding a correction factor of 0.65 (Fig. S14). Hence, the calculated sulfuric acid concentrations from the proxy method were further corrected using this factor. This correction factor could be only approximated for daytime, as the proxy could not capture the diurnal variation of sulfuric acid. Fig. S6 exhibits the calculated sulfuric acid concentration versus $J_{1.7}$ during the long-term observation. Clearly, data from both the long-term observation and the intensive campaign suggest a ternary nucleation (sulfuric acid + dimethyamine + water) in urban Shanghai.

Constrained by the mass resolving power and the unprecedented chemical complexity of detected atmospheric species, it is extremely difficult to assign a formula to each of the organic species. Identified species including HOMs are listed in table S2.

Limit of detection for sulfuric acid dimer and ion-induced clustering

The limit of detection (LOD) for sulfuric acid dimer in CI-APi-TOF was estimated as 1×10^4 molecules cm^3 from high-resolution peak fitting for 30 minute integration time. In addition, when defining the LOD for sulfuric acid dimer ($H_2SO_4 \cdot HSO_4^-$), its formation due to the ion-induced clustering (IIC) within the CI inlet should also be considered.

The concentration of sulfuric acid dimer produced due to IIC has a quadratic dependency on sulfuric acid monomer concentration and a linear dependency on the reaction time within the CI inlet. Following the calculations from the Zhao *et al.* study

(*29*) and the Hanson *et al.* study (*53*), we have estimated the lower detection limit of sulfuric acid dimer as set by IIC. The sulfuric acid dimer due to IIC is defined as follows:

$$[H_2SO_4HSO_4^-]_{IIC} = \frac{k_{21}}{2}\ [H_2SO_4]^2 t \qquad E(3)$$

where k_{21} is the ion-molecule reaction rate coefficient between neutral sulfuric acid molecule and bisulphate ion (HSO_4^-) and t is the reaction time inside the CI inlet. Following the Hanson & Eisele (2002) study (*53*), we have chosen an upper estimate of 2.4×10^{-9} cm^3 s^{-1} for k_{21}, which according to the Zhao *et al.* study (*29*) can be an overestimation by a factor of 2.

During the day time, the detected dimer concentration was well above the lower detection limit due to IIC as well as the LOD. This confirms the detection of real sulfuric acid dimer as a result of a third body (likely amines) evaporating from the cluster upon the ionization (see main text). In contrast with previous observations of sulfuric acid dimer with CI-APi-TOF (*24,27*), we can exclude the contribution of ambient ions to the neutral $H_2SO_4{\cdot}HSO_4^-$ signal because their concentration is much smaller than the total cluster concentration (see Figs. S3b and S4).

SA-DMA clusters were not quantified and their detection limits could not be assessed. Similarly to SA trimer, the detection limit of SA-DMA clusters will depend not only on the instrumental noise, but also on the presence of other molecules at a specific nominal mass in the mass spectra of CI-APi-TOF. It is straightforward to identify SA- and SA-DMA clusters due to the negative mass defect (the difference between the exact mass and the nominal mass of a molecule) of sulfur. However, when the signal of other peaks at the same nominal mass is higher than the signal of SA- or SA-DMA clusters, these peaks cannot be fit as reliably (see Fig. S5). Therefore, compared to a detection limit estimated purely from instrumental noise, the detection limit of these clusters will be higher and will change as a function of time depending on the other ion signals at the same nominal masses.

Cluster kinetics simulations

Cluster kinetics simulations were performed to study kinetically limited SA-DMA nucleation. The simulations were performed using a molecular-resolution cluster kinetics model ACDC (Atmospheric Cluster Dynamics Code) (*54*). Instead of simulating a full multi-component system, a quasi-unary model system containing only one model substance was simulated. The model substance was set to have the properties of a SA-DMA cluster, including one molecule of SA and one molecule of DMA, with a molecular mass of 143 amu and a density of 1500 kg m^{-3}. The model system included species from vapor monomers up to clusters containing 120 molecules, which corresponds to the range from ~0.7 nm to 4 nm in the mass diameter. Temperature was set to 278 K in all the simulations. Previously, simulations with a similar model system have been found to be able to describe particle formation involving SA and DMA in the CLOUD chamber (*6,35*).

To obtain the time-development of cluster concentrations, the discrete General

Dynamics Equation (GDE) was numerically solved for each cluster starting from vapor monomers. Generally, the GDE includes all processes where a cluster can be formed or lost: the production of vapor monomers, all possible collision and evaporations involving vapor monomers and different clusters, and the loss of vapor monomers and clusters due to an external sink. However, in our simulations, evaporation of clusters was not allowed to simulate particle formation at the kinetic limit. The collision rates between different clusters were calculated as hard-sphere collisions from the kinetic gas theory.

The simulations were performed using a constant vapor production rate, which was varied between 5×10^3 and 7.5×10^6 cm^{-3} s^{-1} in different simulations. Four simulations sets were performed with CS values corresponding to observations in Shanghai: CS = 0.01, 0.02, and 0.03 s^{-1}. In addition, one simulation set with a lower CS value was performed: CS = 0.001 s^{-1}. In this simulation set, vapor production rate was varied between 50 and 7.5×10^6 cm^{-3} s^{-1}. The size-dependency of CS was assumed to follow an exponential form, which describes the size-dependency of losses due to pre-existing particle population in the atmosphere.

The simulations were run until a steady state was reached, after which the steady-state concentrations of monomer and dimer were determined from each simulation. Figure 1B illustrates the relationship between monomer and dimer concentrations in four simulations sets with different CS values. In addition, we determined the net particle flux (i.e. particle formation rate J) past 1.7 nm and 3 nm. Fig. S12 shows the ratio between particle formation rates at these sizes ($J_3/J_{1.7}$) determined from measurements and simulations. In the simulations where CS values are similar to observations in Shanghai, $J_3/J_{1.7}$ is lower than measured $J_3/J_{1.7}$. Previously, Kulmala et al. (2017) also showed that in Chinese megacities, the observed survival rate of particles is higher than the survival rate expected based on the theory. They propose that this discrepancy can be explained if molecular clusters are scavenged by pre-existing particles less efficiently than expected, or if the growth rates of molecular clusters are higher than the determined values. In addition, the difference between measured and simulated $J_3/J_{1.7}$ may results from the simple assumptions of our model: vapor production rate and CS are set to constant values and only one model substance is used. In the atmosphere other compounds besides sulfuric acid and DMA may also participate in growing the particles to 3 nm. Overall, the model simulations should be used only for qualitative analysis of the behavior of the system.

Determination of particle formation and growth rates

Classification of nucleation events

New particle formation (NPF) events were identified by bursts of sub-3nm particles and subsequent growth to larger sizes according to PSM and nano-SMPS data. The strong NPF events were defined as events during which the maximum-to-background concentration ratio of sub-3nm particles was larger than 20. Furthermore, during strong

NPF periods, the concentration of sub-3nm particles should maintain a high concentration for several hours and should not significantly fluctuate. With such criterions, 114 strong NPF events were classified out of 731 days with a frequency of 15.6 %. The particle number size distributions of a typical strong NPF events are plotted in Fig. S3a. However, since the meteorological conditions are frequently unstable and the source rates of nucleation precursors in the atmosphere are not always constant in ambient observations, not all strong NPF events behaved in a nice "banana" shape.

In addition to strong nucleation events, there were also a number of weak or undefined events. To investigate the prevailing mechanism of NPF in polluted urban environment, we focused on strong NPF events in this particular study.

Formation rate

The particle formation rates (J_{dp}) were calculated using the following equation (*55*):

$$J_{d_p} = \frac{dN_{d_p}}{dt} + CoagS_{d_p} \times N_{d_p} + N_{d_p} \times \frac{GR}{\Delta d_p} \quad (E4)$$

where $CoagS_{dp}$ is the coagulation sink of particles, N_{dp} is the particle number concentration in the size bin [d_p, d_p+ Δd_p], and GR is the growth rate in the same size bin. It should be noted that E(4) does not account for the effects of self-coagulation on particle growth and size-dependency of GR. $CoagS_{dp}$ for particles with a certain diameter d_p can be calculated from the number size distribution measured by two SMPSs:

$$CoagS_{d_p} = \sum_{d_p}^{d_p'} K(d_p, d_p')N_{d_p} \quad (E5)$$

where K (d_p , d_p') is the coagulation coefficient between particles of d_p and d_p' sizes and N_{dp} is the particle concentration in the size bin [d_p , d_p']. From a previous study, the relation between total condensation sink (*CS*) and $CoagS_{dp}$ is as follows (*56*):

$$CoagS_{d_p} = \mathrm{CS} \times (d_p/0.71)^m \quad (E6)$$

where the exponent m is ~1.6.

Condensation sink (CS) describes the condensing vapor sink caused by the particle population (*55*):

$$\mathrm{CS} = 2\pi D \sum_{d_p} \beta_{m,d_p} d_p N_{d_p} \quad (E7)$$

where D is the diffusion coefficient of the condensing vapor (usually assumed to be sulfuric acid), and $\beta_{m,dp}$ is the transitional regime correction factor.

The nucleation rate ($J_{1.7}$) was calculated from the size range [1.7 nm, 2 nm] of PSM. The formation rate (J_3) was obtained from the size bin [3 nm, 7 nm] of nano-SMPS. An

inter-comparison of J_3 determined from NAIS and nano-SMPS is shown in Fig. S15, showing a good agreement. This suggests that data from NAIS and nano-SMPS were comparable with each other.

In comparison to the neutral particle concentration, the ion concentration was very low during NPF periods (Figs. S3b and S4). We calculated the ion formation rate to determine the ion-induced formation rate contribution, using the following equation:

$$J_{dp}^{\pm} = \frac{dN_{dp}^{\pm}}{dt} + CoagS_{d_p} \times N_{dp}^{\pm} + N_{dp}^{\pm} \times \frac{GR}{\Delta d_p} + \alpha \times N_{dp}^{\pm} \times N_{<dp}^{\mp} - \chi \times N_{dp} \times N_{<dp}^{\pm} \qquad (E8)$$

where the polarity of the ions is indicated by a negative (-) or positive (+) superscript. The ion concentration is determined for ions with a diameter size of d_p, or sizes smaller than < d_p. The ion-ion recombination coefficient is taken as $\alpha = 1.6\times10^{-6}$ cm^3 s^{-1}. The last term in the equation (E8) determines the ion-aerosol attachment with a coefficient $\chi = 0.01\times10^{-6}$ cm^3 s^{-1}(*55*).

The ion induced contribution to new particle formation is taken as the ratio between $J_{1.7}$(ion)/$J_{1.7}$(total), using the same size range of 1.7 nm to 2 nm for d_p.

Growth rate

The growth rate (GR) of a particle is defined as the rate of change of its diameter. The maximum-concentration method was adopted to determine particle growth rates for different diameter ranges based on PSM, NAIS and nano-and long-SMPS data (*22,57*). The time evolution of each size bin was fitted by Gaussian function and the times of maximum-concentration of each size bin were obtained from the fit. The growth rates were determined as the slopes of the linear fits to the diameter-versus-time data.

The initial growth rate of freshly formed particles ($GR_{<3\ nm}$) were obtained from PSM data. In addition, $GR_{<3\ nm}$ was determined from ion size distributions measured with the NAIS for the events for which we had NAIS data. Subsequent growth rates of bigger particles ($GR_{3\text{-}7\ nm}$ and $GR_{7\text{-}25\ nm}$) were calculated from PSM and nano-and long-SMPS data for all the events, and from NAIS ion and particle mode data for the events for which we had NAIS data. Fig. S3a illustrates growth rate calculations using different instruments for a NPF event on 16 February. Figure S9 shows the statistics of GR in different size ranges during long-term measurements.

The measured GRs are subject to uncertainties caused by uncertainties in particle size distribution measurements and the effects of other dynamic processes besides particle growth on the time-evolution of particle size distribution. In previous studies the systematic error in GR has been estimated to be ~50% for sub-3 nm particles and ~25% for larger particles (*43, 57*).

To study the sensitivity of $J_{1.7}$ to uncertainties in $GR_{<3\ nm}$ values, we calculated $J_{1.7}$ for each event during the intensive measurement period with $GR_{<3\ nm}$ = 0.1 nm/h and

$GR_{<3\ nm}$ = 10 nm/h. The range of $J_{1.7}$ corresponding to these GR values is shown in Fig. S16 with vertical bars. It can be seen that our results on $J_{1.7}$ are not strongly affected by uncertainties in determined GRs.

Modelled growth rate

We determined GR from cluster kinetics simulations to study if the observed sub-3 nm particle growth can be explained when accounting for the contribution of SA-DMA clusters to the growth. We calculated the median sulfuric acid and CS for the events during the intensive measurement campaign (1.3×10^7 cm^{-3} and 2.1×10^{-2} s^{-1}) and performed a model simulation using these values and two additional simulations by assuming ±50% uncertainty in sulfuric acid concentration. Then we determined GR from these simulations. First, simulated clusters were divided to linearly spaced size bins with a width of 0.1 nm. Then, the appearance time t_{app} was determined for each size bin with the mean diameter D_p by determining the time when the concentration in each size bin reached 50% of the total increase in the concentration. Finally, GR was obtained by applying a linear fit to (t_{app}, D_p) data for the size range between 1 and 2 nm.

In addition, growth rates due to sulfuric acid monomer condensation were estimated following the method described by Nieminen *et al.* (*58*) and are presented in Fig. S10. The upper limit of growth as explained by the condensation of organic species detected by CI-APi-TOF was also estimated (Fig.S10). Concentrations of detected organics were determined from the high resolution-fitted peaks with positive mass defect in range 190-500 Th. The concentration of organics was calculated using the same calibration coefficient as for sulfuric acid (see equation E(1)). In the model, the density and the mass of H_2SO_4 were 1830 kg m^{-3} (liquid phase density of sulfuric acid) and 98 g mol^{-1}, respectively. The density for organics was assumed to be 1500 kg m^{-3} and the average molar mass for organics was taken as 250 g mol^{-1}, which excluded the reagent ion mass. In a sensitivity test for organic molar mass, the modelled growth rate increased by 23% when molar mass was changed from 250 to 350 in the size range 1-3 nm and decreased by 25% when mass was changed to 170 g mol^{-1}. Taking into account the uncertainties in determining the concentration and density of the detected organics, 250 g mol^{-1} was chosen as a good approximation. The uncertainty of the modelled GR was estimated from the ±50% uncertainty in sulfuric acid and organic concentrations.

Contribution of newly formed particles to the total particles

The number of new particles with 30 nm diameter formed from atmospheric nucleation under the boundary layer during the two-year observation in Shanghai was assessed by the following equation:

$$\mathrm{N}_{30nm} = \mathrm{J}_{30} \times \mathrm{T}_N \times \mathrm{N}_D \times \mathrm{F}_N \times S_A \times \mathrm{BL}_H \qquad (E9)$$

where J_{30} is the median formation rate of 30 nm particles derived from E(10) using measured J_3, CS and GR (*17*), T_N is averaged NPF duration for each event day, N_D is number of total observation days, F_N is the frequency of event days, S_A is area of Shanghai, and BL_H is averaged height of boundary layer. Actually, we used values of 6 cm^{-3} s^{-1} for J_{30}, 4 hours for T_N, 365 days (one year) for N_D, 15.6% for F_N, 1 square kilometre for the area and 1 km for BL_H.

The relationship between the particle formation rate J_3 and J_{30} was according to the Kerminen and Kulmala study (2002) (*17*):

$$J_{30} = J_3 \exp\left[0.23 \frac{CS'}{GR'}\left(\frac{1_{nm}}{30_{nm}} - \frac{1_{nm}}{3_{nm}}\right)\right] \qquad (E10)$$

where $CS' \approx$ CS/(10^{-4} s^{-1}), GR′= GR/(1 nm $hour^{-1}$).

The primary emissions were calculated with the GAINS model (Greenhouse gas – Air pollutant Interactions and Synergies (*59*)) by applying the recently implemented particle number emission factors (*36*). In GAINS, the emissions are initially calculated for countries or regions, in terms of China for provinces. The provincial emissions are calculated by multiplying the activity data for different human activities with the source-, technology- and, if applicable, fuel-specific emission factors. The activity levels are received from international organizations (IEA, OECD, UN) and national statistics, whereas the emission factors are retrieved from scientific literature and emission databases. The provincial emissions are further gridded to 0.5 deg × 0.5 deg resolution. The gridded total particle number emissions in and nearby China are presented in Fig. S11. The values presented in the main article are for the nine grid cells indicated with a rectangle in Fig. S11 (5×10^{21} km^{-2} $year^{-1}$) and for the grid cell with the highest emissions in the middle of the rectangle (2×10^{22} km^{-2} $year^{-1}$).

Figures

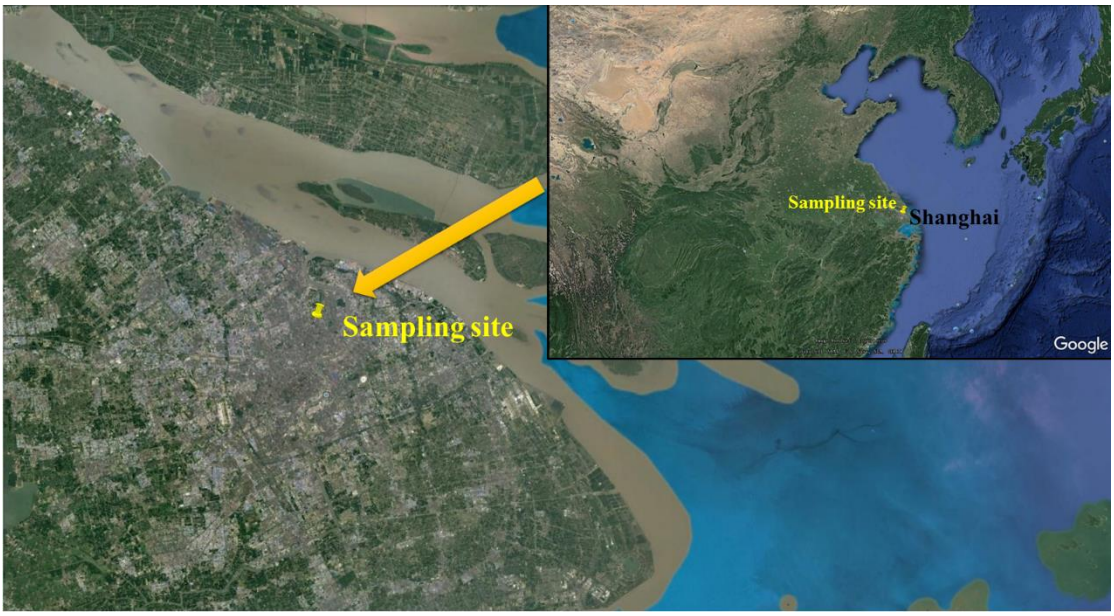

Fig. S1: Google map of the Fudan site that is a representative urban station.

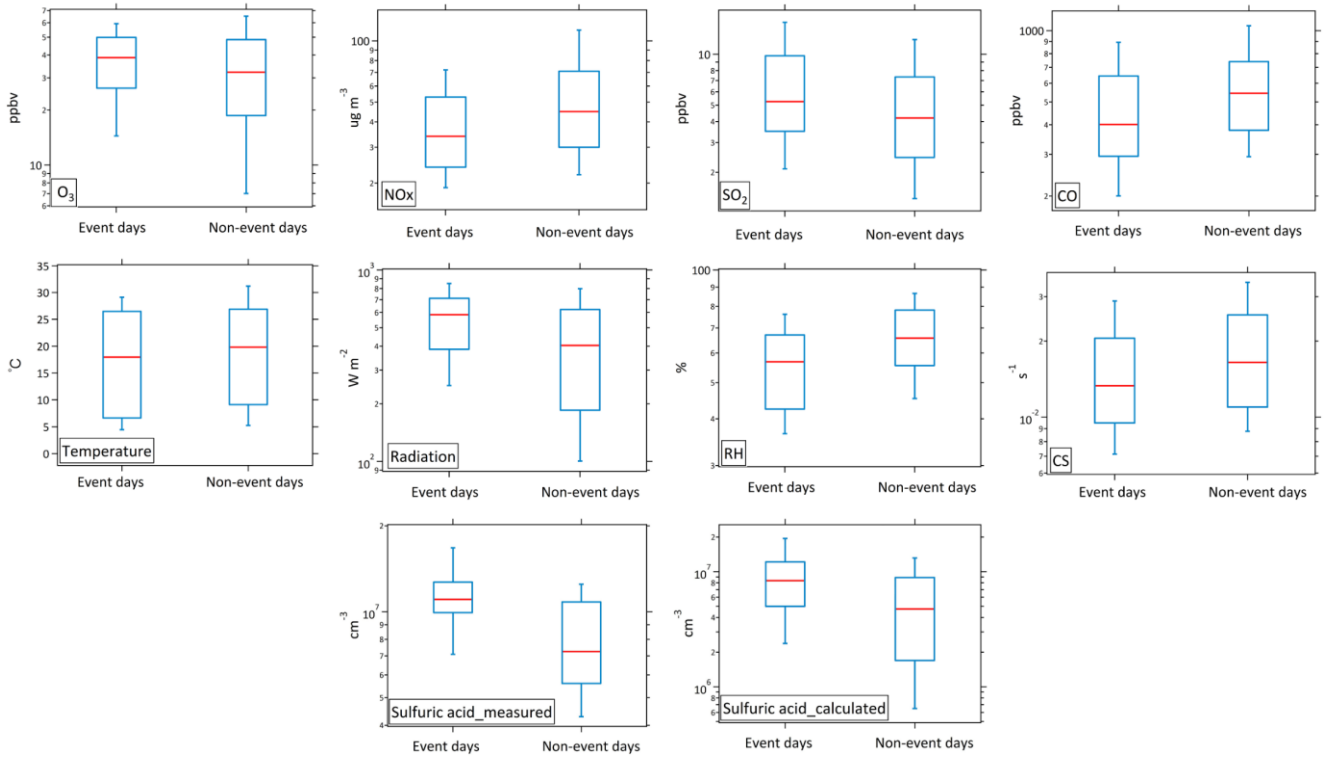

Fig. S2: Comparison of concentrations of trace gases (O_3, NO_x, SO_2 and CO), condensation sink (CS), meteorological parameters and measured and calculated sulfuric acid concentrations between NPF event and non-event days. Rainy days were excluded according to the precipitation measurement. The horizontal red lines indicate the median; the blue boxes show the range from the 25th to 75th percentile; and the whiskers present the range from the 10th (low) to 90th percentile (top). For event days, data were averaged between the beginning and the peak time of each event. For non-event days, data were selected from 09:00 to12:00 am (local time).

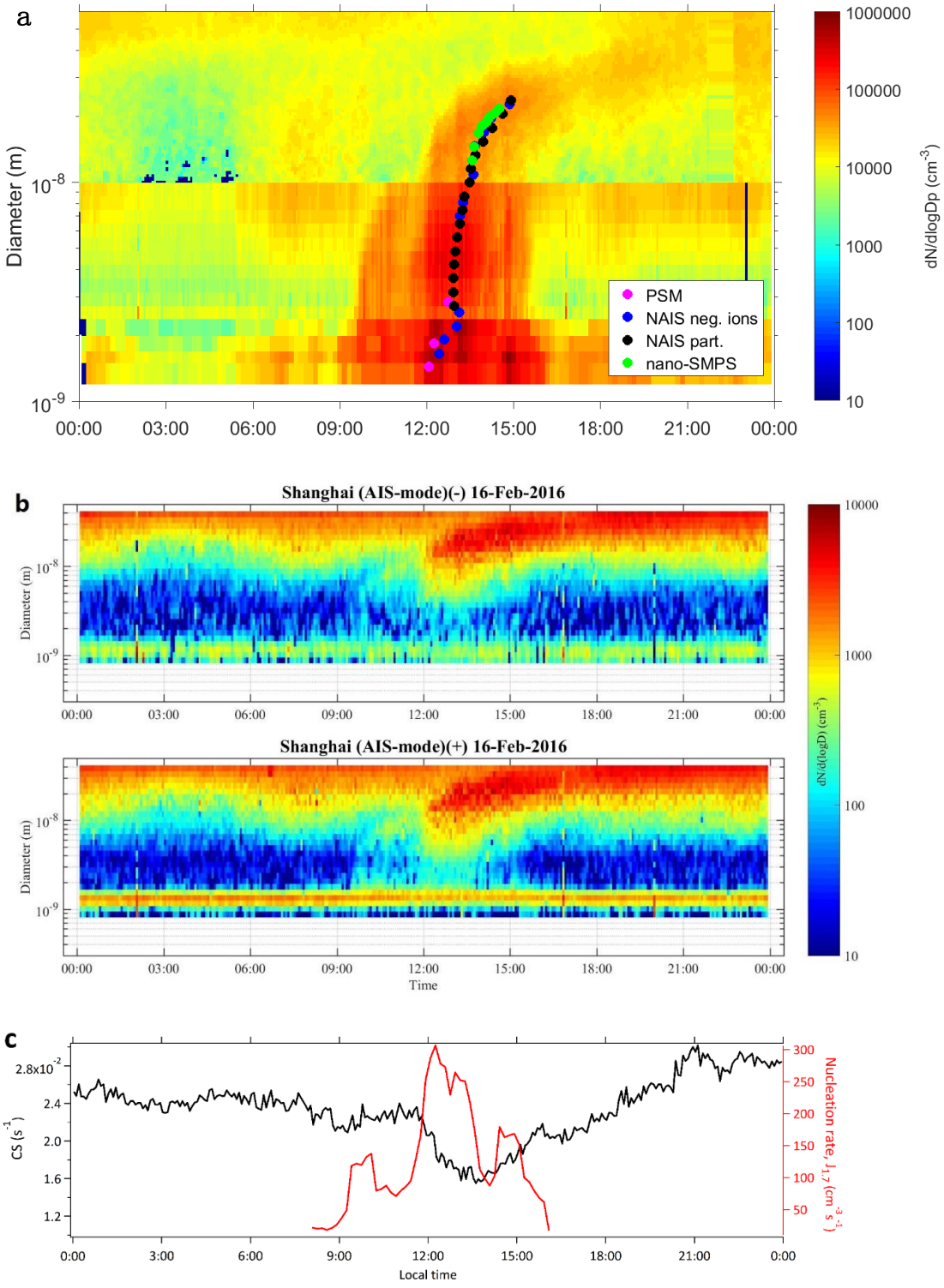

Fig. S3: Particle number size distributions and naturally charged ions during a typical NPF event day on 16th February, 2016. (**a**) Particle number size distributions measured by PSM, NAIS and SMPS. The colored circles show the data points used for calculating particle growth rate from different instruments. (**b**) Air ion size distributions

measured by NAIS. Upper and lower panels show the time evolution of negative and positive ions, respectively. Sub-3 nm air ion concentrations were very low because they were scavenged by the high condensation sink in Shanghai. Hence, the contribution of ion-induced nucleation to NPF was insignificant. **(c)** Time series of nucleation rate ($J_{1.7}$) and condensation sink (CS).

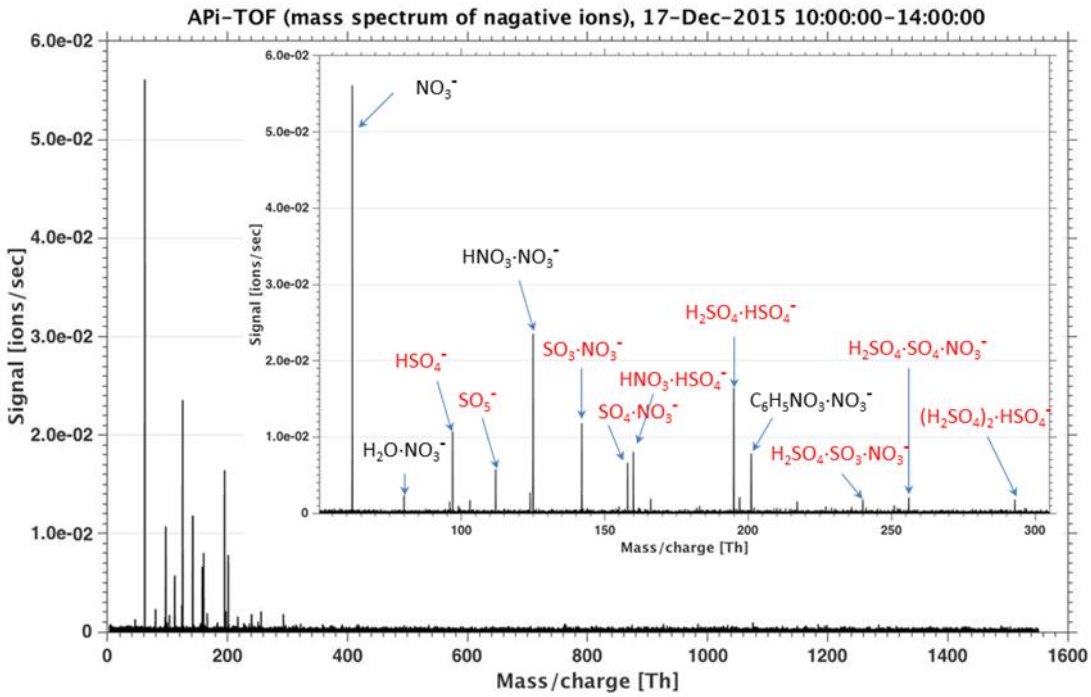

Fig. S4: A typical APi-TOF mass spectrum of negative ions during a strong new particle formation event, 10:00-14:00, 17th December, 2015. The ion concentration was very low. The negative ions were mainly nitrates and molecules/clusters containing sulfur and oxygen. There were no detectable ions/clusters with *m/z* > 300 likely because of the large condensation sink.

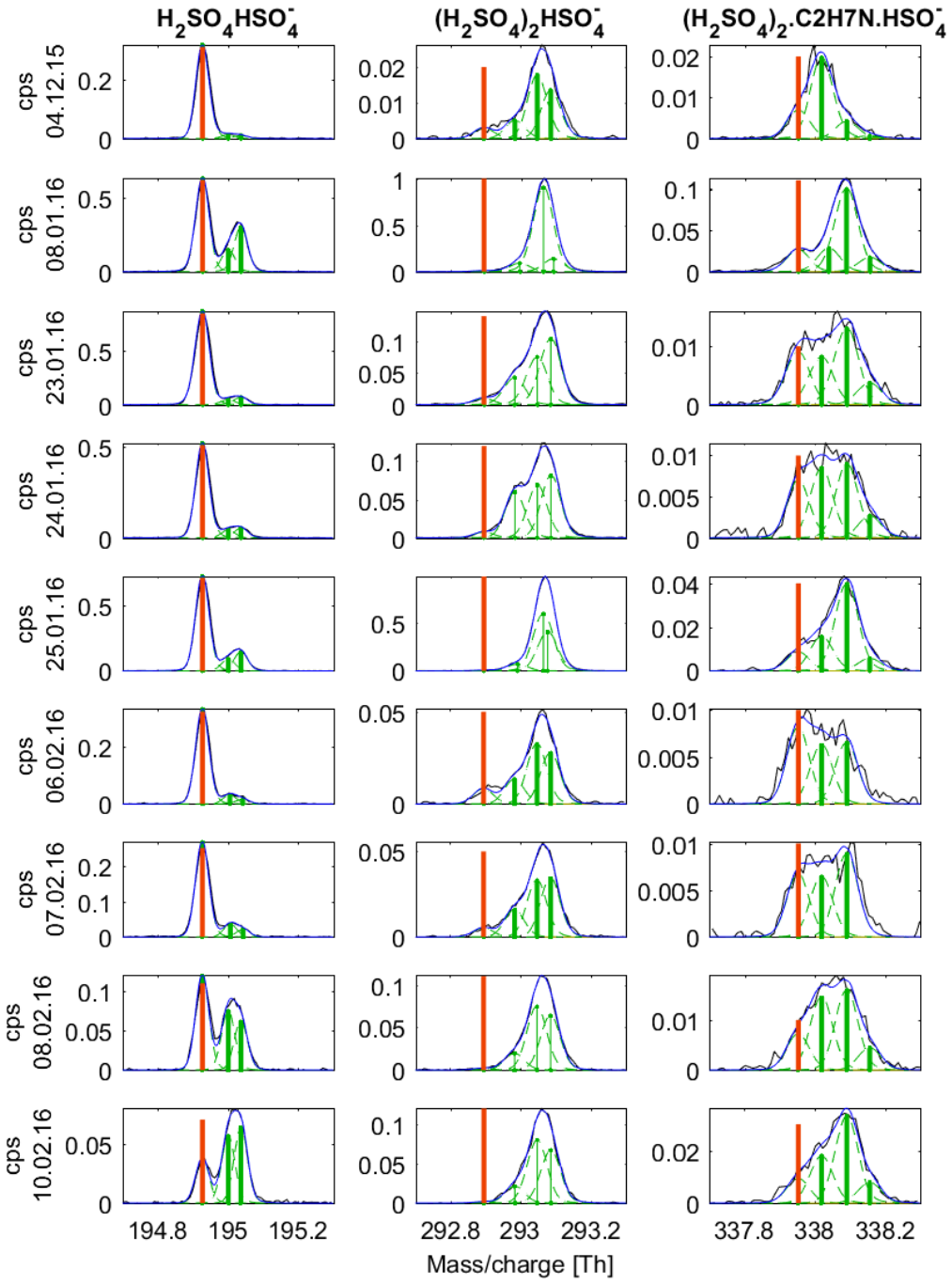

Fig. S5. High-resolution peak fits of SA dimer, SA trimer and 3SA-DMA cluster for all 9 NPF events measured by CI-APi-TOF during the intensive campaign. The orange bars show the exact mass of SA dimer, SA trimer and 3SA-DMA cluster. Other compounds, found using peak search method in tofTools software (version 607), are marked as green bars. The black curve and the blue curve indicate measured values and sum of fitted peaks respectively. The label of Y-axis is counts per second (cps) and date

(day-month-year). On 8th of January, 25th of January, 8th and 10th of February, the figure suggests that no SA trimer was observed. However, on those day the signal of the other peaks at m/z 293 were especially high, and therefore the SA trimer peak becomes much harder to distinguish from the tails of the larger peaks, even if its concentration had been similar to the other NPF days (see also Materials and Methods).

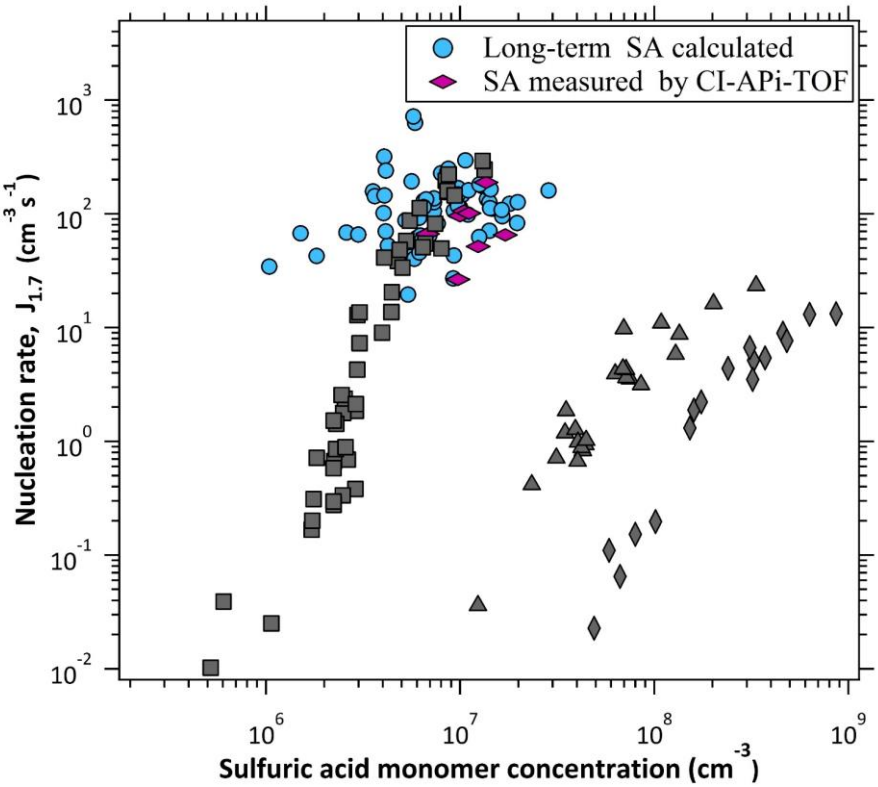

Fig. S6. Ambient and CLOUD nucleation rates against sulfuric acid monomer concentration. Grey diamonds, triangles, and squares denote CLOUD data for H_2SO_4-H_2O, H_2SO_4-NH_3-H_2O, and H_2SO_4-DMA-H_2O nucleation, respectively, at 38% RH and 278K. Purple diamonds show data points during NPF events between December 2015 and February 2016 with sulfuric acid concentrations measured with CI-APi-TOF, whereas blue circles denote ambient data points between March 2014 and November 2015 with sulfuric acid concentrations calculated from the proxy. In this plot, sulfuric acid concentrations were averaged values between the beginning and the peak time for each event.

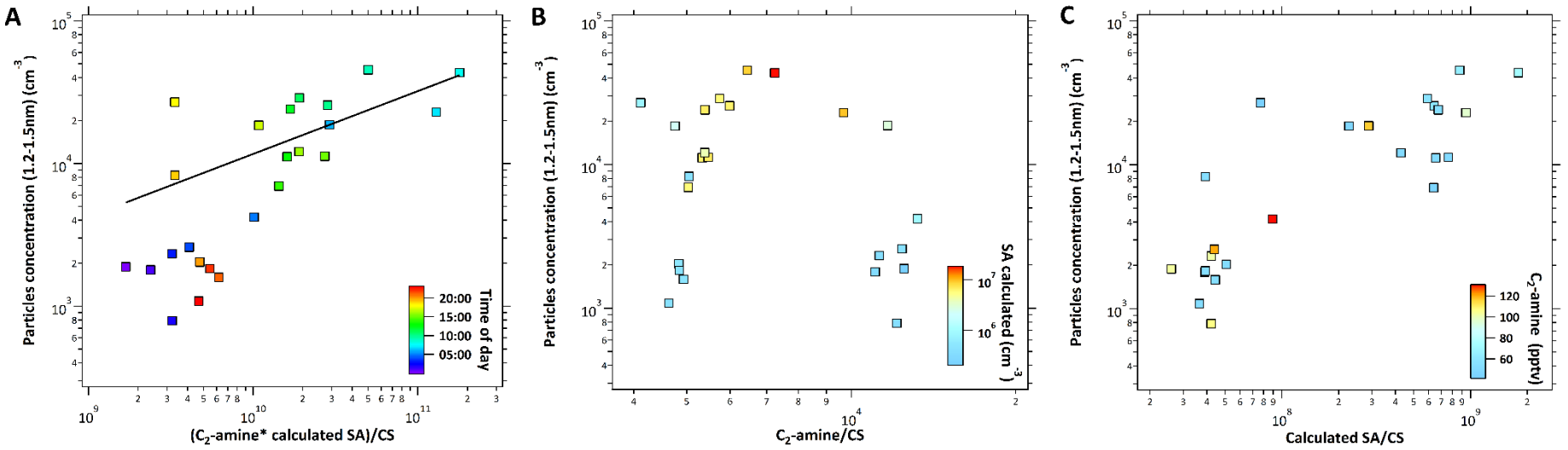

Fig. S7. Correlation of concentrations of small particles (1.2-1.5 nm in diameter) with [(C_2-amine*SA calculated)/(condensation sink)], [C_2-amine]/CS, and [calculated SA]/CS, respectively. The data points correspond to hourly-average values during a strong new particle formation event on 12th August, 2015. The black line is the fitting line using power function ($y=a*x^b$) and the coefficient *a* and *b* are 0.33 and 0.45, respectively. The correlation coefficient r is 0.73.

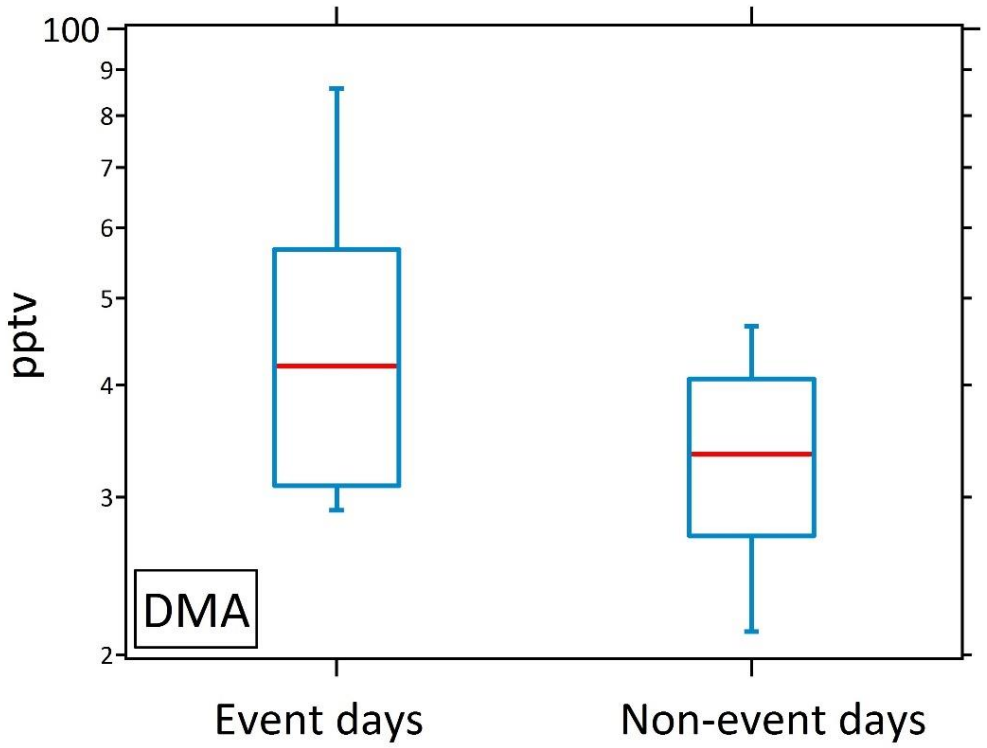

Fig. S8: **Comparison of DMA concentration (between July 2015 and August 2015) between NPF event and non-event days.** For event days, data were averaged between the beginning and the peak time of each event. For non-event days, data were selected from 09:00 to 12:00 am (local time). The horizontal red lines indicate the median; the blue boxes show the range from the 25th to 75th percentile; and the whiskers present the range from the 10th (low) to 90th percentile (top). Note that NPF events in addition to the strongest ones as defined in the main text have been included for this DMA plot to add more statistics since there were only two strong NPF events (during which DMA concentrations were 40.3 and 80.7 parts per trillion by volume, respectively) in the one-month measurements of DMA. Additional NPF events included in this particular plot are defined as events with maximum-to-background concentration ratios for sub-3 nm particles being between 10 and 20.

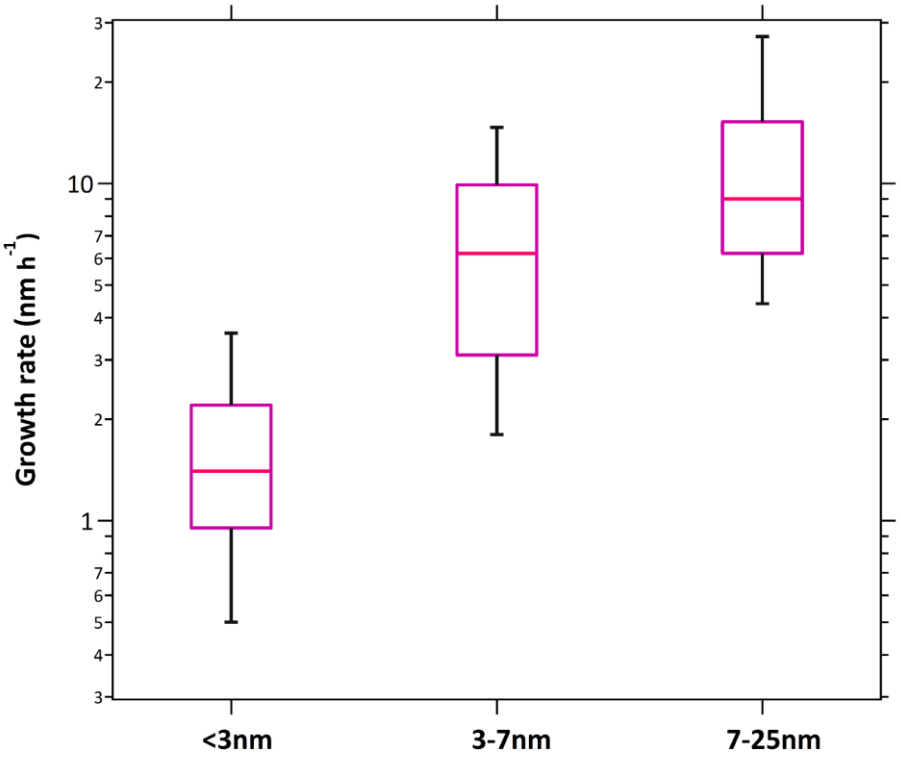

Fig. S9: **Size-resolved growth rates from long-term observation.** The horizontal pink lines indicate the median; the purple boxes show the range from the 25th to 75th percentile; and the whiskers present the range from the 10th (bottom) to 90th percentile (top).

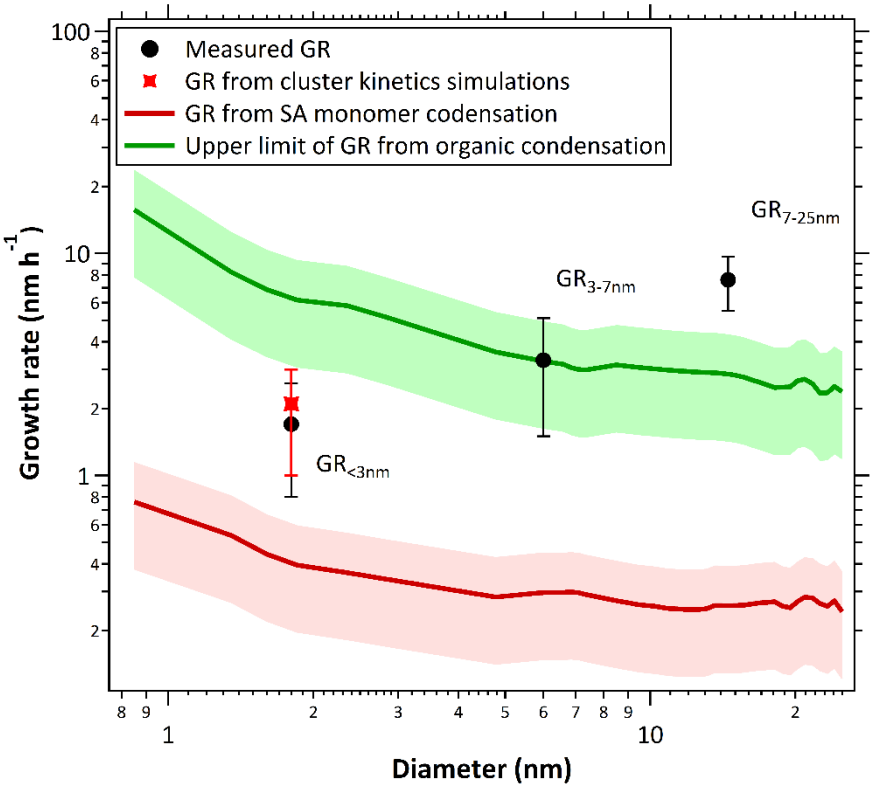

Fig. S10. Observed and modelled growth rate (GR) on an example new particle formation day of on 24th January, 2016. In addition to measured GR, we have also estimated the growth of aerosol particles due to condensation of sulfuric acid monomer as well as the upper limit of growth explained by the condensation of organic species observed by CI-APi-TOF which were assumed non-volatile following the method described by Nieminen et al. (2010) (*58*). Also, we have included the $GR_{<3nm}$ as simulated by kinetically-limited model (see Material and Methods) for conditions of 24 Jan 2016 (CS $\approx$ 0.01 s^{-1}, $[H_2SO_4]$ = ~6.8×10^6 molecule cm^{-3}).

The growth rates, as shown by black circles in the figure, were calculated for the following diameter ranges: < 3 nm, 3-7 nm, and 7-25 nm. The red cross marker shows $GR_{<3nm}$ determined from cluster kinetics simulations. The black error bars indicate the total uncertainty of measured GR, which was defined as $\sqrt{((\text{error of the linear fit})^2 + (\text{systematic uncertainty of GR})^2 * (\text{GR})^2)}$. The systematic uncertainty on $GR_{<3\ nm}$ and $GR_{>3nm}$ was assumed to be 50% and 25%, respectively, as suggested previously by Tröstl et al. (2016) and Yli-Juuti et al. (2011) (*35,57*). The dark red line indicates GR calculated assuming SA monomer condensation, and the red shadow shows the uncertainty that is derived from 50% uncertainty in the concentration of sulfuric acid. The dark green line indicates the upper limit of GR

calculated by condensation of organics measured by CI-APi-TOF, and the green shadow shows the uncertainty that is derived from 50% uncertainty in the concentration of measured organics.

On this particular day, the condensation of sulfuric acid monomer can only explain a fraction of growth of particles below 3nm. However, the $GR_{<3nm}$ from cluster kinetics simulations of SA-DMA system can predict the observed growth within experimental errors. The upper limit of organic condensational growth overestimates the $GR_{<3nm}$, which shows that not all of the organic species observed by CI-APi-TOF in Shanghai are able to condense onto sub-3nm clusters. While the observed $GR_{3\text{-}7nm}$ can be explained by organic condensation, the total contribution to the growth is likely to be lower due to the low- and semi- volatility of some of the detected species. For larger sizes, however, it is clear that the observed organics by CI-APi-TOF cannot account for all the growth. Therefore, there are other species that contribute to growth only at larger sizes, likely other semi-volatile organics that remain undetected by CI-APi-TOF. The abundance of such organics from oxidation of volatile organic compounds (VOCs) in the polluted Shanghai can be expected (*37*).

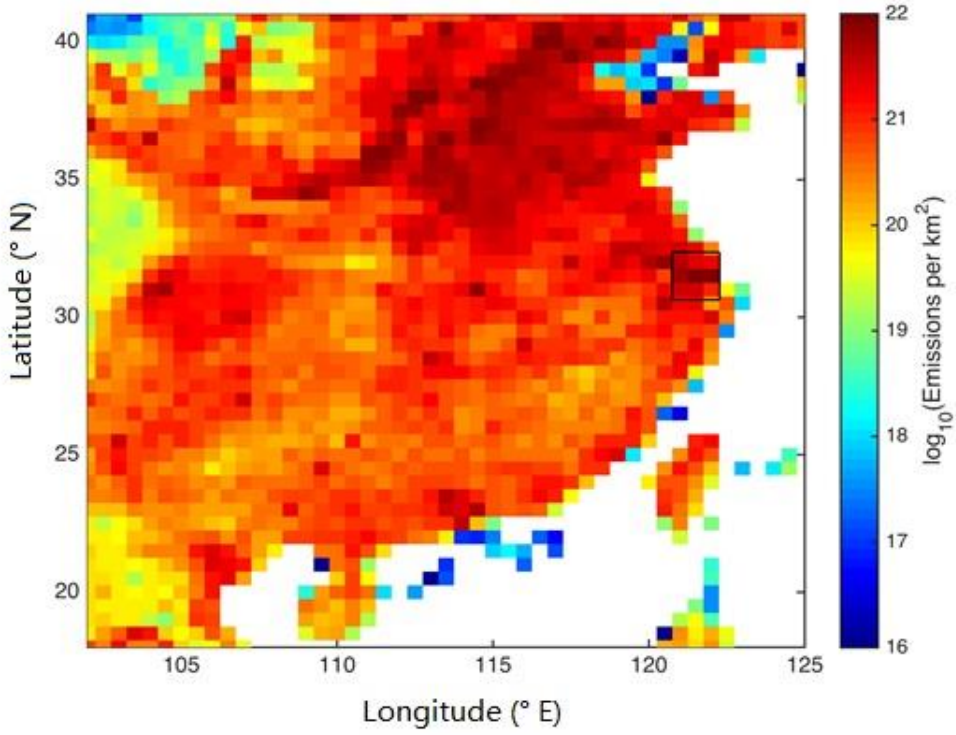

Fig. S11. Total anthropogenic direct aerosol particle number emissions for 2010 over China, as derived from the GAINS model. The grid cells applied in this study are indicated with a black square. Note that in the present manuscript, NPF was studied only within the Shanghai metropolitan area, and thus the estimated new particle formation rates (5×10^{21}km^{-2}y^{-1}) should be compared only to the emissions presented within the domain of the 9 indicated pixels.

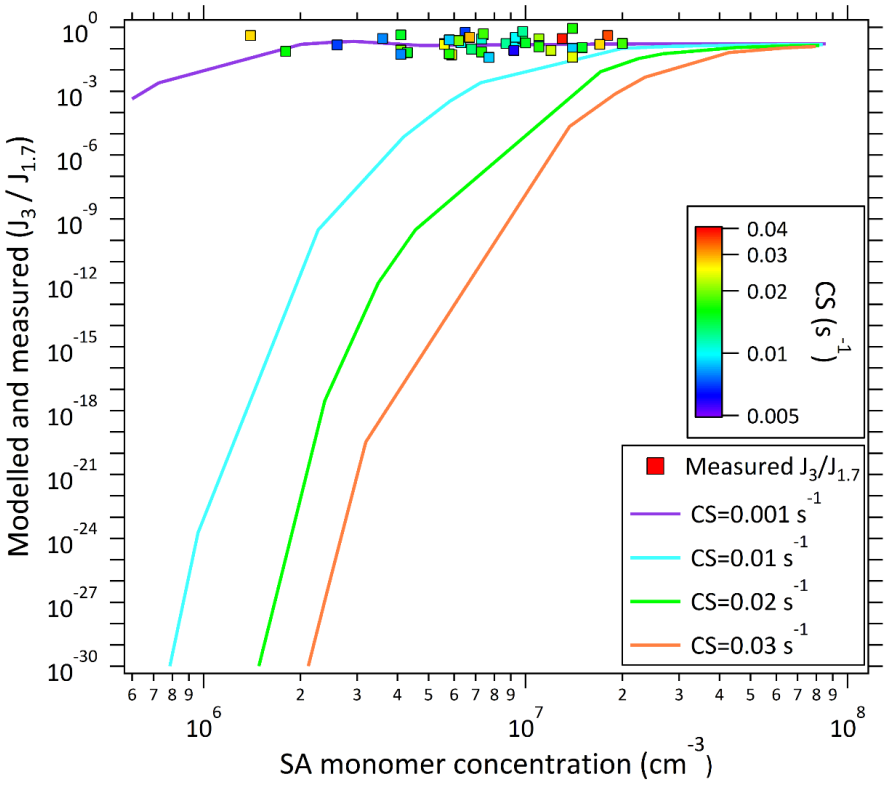

Fig. S12. Measured and modelled J_3-to-$J_{1.7}$ ratios at different sulfuric monomer concentrations and CS values. The measured values are averaged values between the beginning and the peak time of each NPF event during our two-year long-term measurements period. Since a number of J_3 or $J_{1.7}$ and calculated SA monomer concentrations were not available during the 114 events, there were only 44 data points. The modelled values are obtained from cluster kinetics simulations of a kinetically limited SA-DMA system. The modelled J_3-to-$J_{1.7}$ ratios are lower than measured ones at similar CS values, which indicates that our understanding on new particle formation in highly polluted environments is still incomplete (*15*).

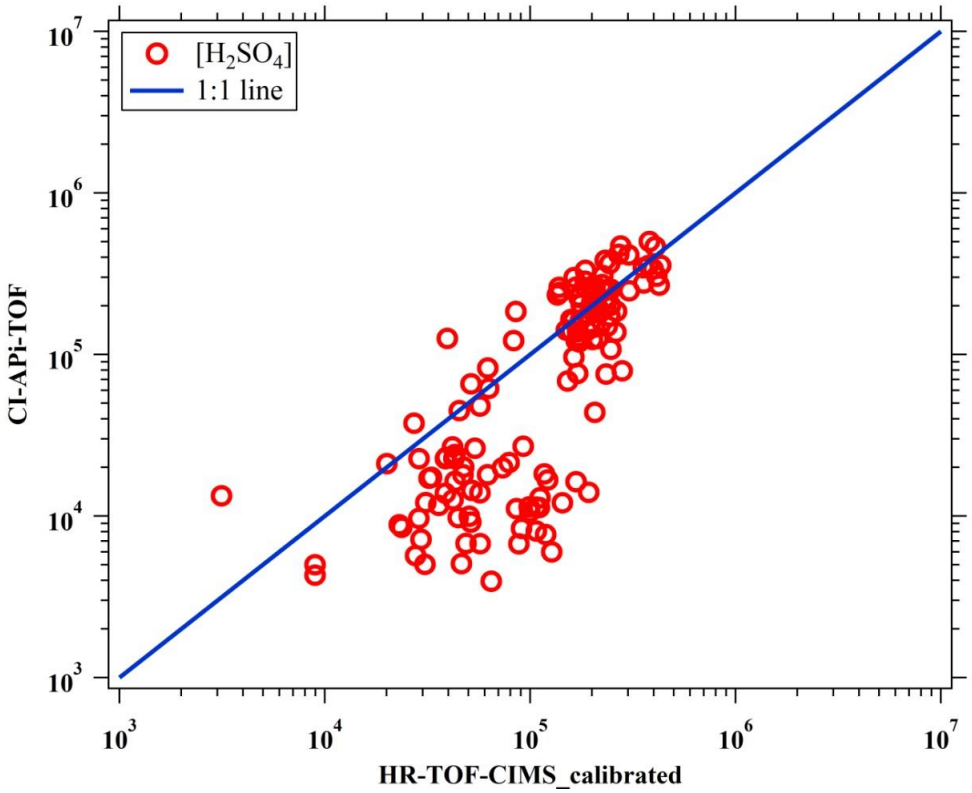

Fig. S13. Inter-comparison of sulfuric acid concentrations measured by CI-APi-TOF and another parallel HR-ToF-CIMS that has been calibrated for H_2SO_4. A calibration coefficient ($C = 6\times10^9$) was used to quantify sulfuric acid concentration for CI-APi-TOF. This factor has taken diffusion loss in the sampling line of CI-APi-TOF into account. The data points were 15-min averages for two days.

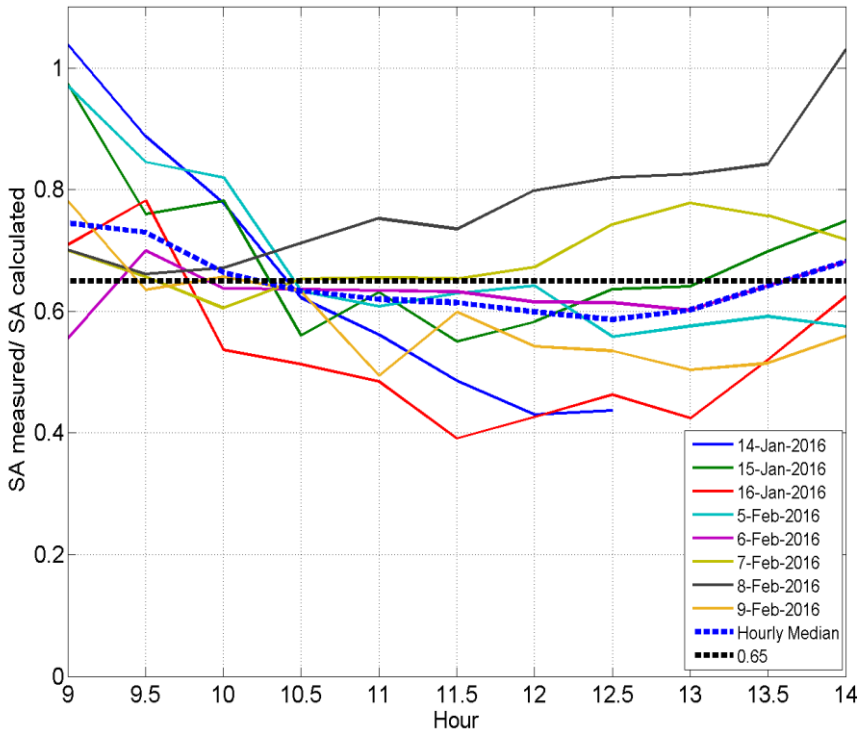

Fig. S14. Ratio of measured-to-calculated sulfuric acid (SA) concentration. Since almost all nucleation events occurred from the late morning to the middle day, a correction factor 0.65 was obtained from the inter-comparison during the day time periods (09:00-14:00 am, local time).

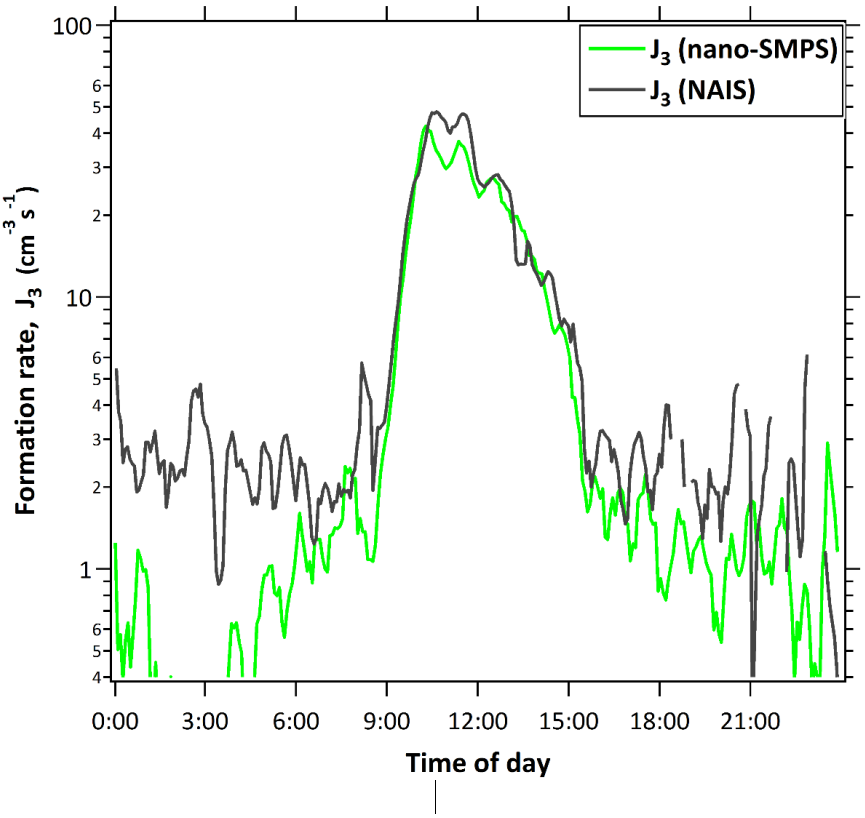

Fig. S15. Inter-comparison of J_3 from different particle measurement instruments (nano-SMPS and NAIS) for 10th of February 2016.

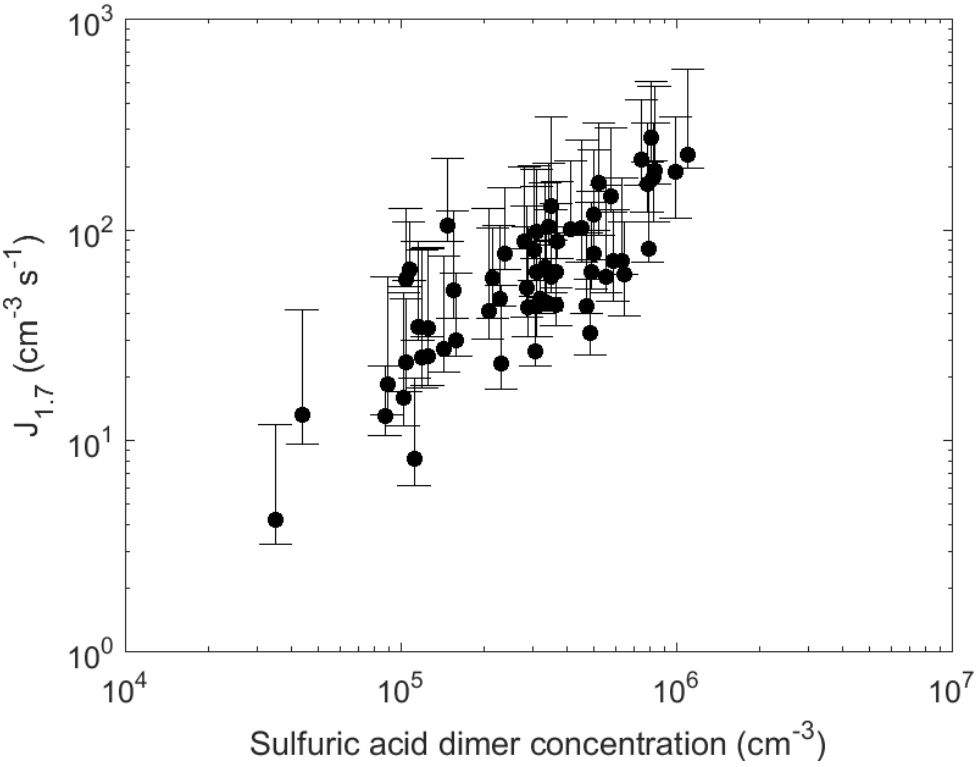

Figure. S16. Sensitivity of the nucleation rate $J_{1.7}$ to sub-3 nm particle growth rate ($GR_{<3\ nm}$). The vertical bars show $J_{1.7}$ calculated with $GR_{<3\ nm}$ = 0.1 nm/h (lower limit) and $GR_{<3\ nm}$ = 10 nm/h (upper limit).

Tables

Table S1. Date of strong NPF events, formation rates ($J_{1.7}$ and J_3), growth rates ($GR_{<3nm}$, $GR_{3\text{-}7nm}$ and $GR_{7\text{-}25nm}$), condensation sink (CS), sulfuric acid concentration, dimethylamine concentration when measured, temperature and relative humidity.

Date (day-month-year)	$J_{1.7}$ [a] ($cm^{-3}\ s^{-1}$)	J_3 [a] ($cm^{-3}\ s^{-1}$)	$GR_{<3\ nm}$ ($nm\ h^{-1}$)	$GR_{3\text{-}7\ nm}$ ($nm\ h^{-1}$)	$GR_{7\text{-}25\ nm}$ ($nm\ h^{-1}$)	CS[b] ($10^{-2}\ s^{-1}$)	Sulfuric acid (cm^{-3})	Dimethylamine (pptv)	Temperature (℃)	Relative humidity （%）
26-02-2014	NA	NA	NA	3.8	5.7	NA	NA		NA	NA
03-03-2014	67.8	NA	2.2	NA	4.5	1.5	NA		7.2	67.2
05-03-2014	100.8	7.0	1.1	4.1	5.1	1.7	7.3E+6 [c]		10.7	42.9
13-03-2014	83.4	30.5	1.9	11.7	NA	3.1	NA		6.3	56.1
14-03-2014	135.1	NA	2.9	1.3	6.11	3.8	1.4E+7 [c]		7.4	41.5
15-03-2014	176.0	51.7	1.2	7.1	10.3	3.8	1.3E+7 [c]		8.0	65.3
21-03-2014	NA	NA	2.8	NA	8.9	1.4	NA		9.9	34.9
04-04-2014	NA	120.6	NA	12.8	7.4	2.6	NA		NA	NA
06-04-2014	105.3	48.8	2.9	3.7	6.1	1.6	7.4E+6 [c]		12.3	36.4
14-04-2014	166.8	69.3	2.3	11.1	15.8	2.7	1.4E+6 [c]		20.5	41.9
22-04-2014	NA	NA	NA	NA	12.5	1.6	NA		20.2	35.3
29-04-2014	122.6	50.2	1.0	15.8	18.9	3.5	1.8E+7 [c]		20.6	51.4
05-05-2014	318.6	140.0	1.8	6.5	7.2	1.5	4.1E+6 [c]		15.7	43.2
07-05-2014	146.8	NA	4.8	10.4	14.0	2.8	1.0E+7 [c]		21.4	42.8
22-05-2014	61.5	NA	1.3	3.8	20.4	1.9	6.0E+6 [c]		25.3	54.6
23-05-2014	19.5	NA	0.6	7.5	17.6	1.3	5.4E+6 [c]		22.8	64.8
26-05-2014	65.0	NA	1.3	4.6	10.5	2.1	7.0E+6 [c]		25.5	67.6
28-05-2014	NA	NA	0.7	NA	NA	NA	9.8E+6 [c]		30.7	34.1
10-06-2014	NA	NA	NA	NA	7.4	1.0	NA		26.3	60.2

11-06-2014	113.2	NA	1.2	NA	58.3	1.3	1.0E+7 [c]		26.2	52.1
08-07-2014	148.2	42.1	1.5	12.2	14.2	1.1	9.8E+6 [c]		28.4	60.8
26-07-2014	630.8	32.0	0.5	5.5	45.2	2.4	5.9E+6 [c]		31.4	58.9
31-07-2014	41.9	7.3	1.0	16.1	NA	0.8	5.6E+6 [c]		31.0	65.5
15-08-2014	42.7	3.2	1.1	6.7	13.4	1.6	1.8E+6 [c]		26.1	NA
30-08-2014	71	7.2	0.4	1.7	11.2	0.9	1.4E+7 [c]		29.2	70.7
31-08-2014	716.2	40.0	2.3	10.4	37.3	1.7	5.8E+6 [c]		28.2	78.6
01-09-2014	734.4	NA	1.5	5.3	6.4	1.9	NA		NA	NA
06-09-2014	227.0	NA	2.1	39.2	10.9	1.0	8.0E+6 [c]		29.6	70.2
11-09-2014	248.9	42.9	1.4	13.7	8.9	1.2	8.7E+6 [c]		27.7	63.2
14-09-2014	157.6	46.9	2.7	6.3	9.1	0.8	3.6E+6 [c]		25.5	77.9
15-09-2014	126.1	35.5	0.6	8.6	4.6	1.1	7.3E+6 [c]		25.9	71.8
17-09-2014	142.9	NA	2.1	NA	9.3	1.0	3.6E+6 [c]		26.2	66.9
20-09-2014	NA	NA	2.3	2.4	8.7	NA	NA		24.5	78.1
06-10-2014	NA	NA	NA	7.6	7.4	1.2	NA		22.5	60.1
13-10-2014	64.6	NA	3.6	8.1	15.6	0.9	NA		NA	NA
14-10-2014	100.1	27.3	2.8	5.6	31.1	1.8	NA		20.4	45.8
15-10-2014	160.3	NA	3.3	6.6	7.2	2.4	2.9E+7 [c]		20.3	36.9
28-10-2014	NA	34.3	NA	8.9	23.7	0.7	NA		20.5	65.9
02-11-2014	NA	28.0	NA	4.8	18.9	1.2	NA		16.8	73.0
03-11-2014	111.3	12.5	2.2	4.3	7.8	1.5	1.5E+7 [c]		13.9	55.6
06-11-2014	NA	NA	0.6	0.9	12.5	2.7	NA		19.0	62.8
07-11-2014	33.2	NA	0.7	7.8	2.0	0.9	NA		17.4	65.0
09-11-2014	82.0	3.2	0.4	1.1	2.6	0.9	7.7E+6 [c]		17.3	63.3
13-11-2014	64.4	12.2	1.0	2.3	5.1	1.0	6.3E+6 [c]		13.3	46.7
01-12-2014	67.4	NA	0.4	23.5	5.6	1.1	1.5E+6 [c]		6.4	37.8

02-12-2014	NA	NA	NA	3.7	29.8	1.3	NA		6.3	43.2
04-12-2014	95.3	NA	1.4	3.2	4.7	1.3	1.7E+7 [c]		5.3	46.9
05-12-2014	126.2	112.9	1.5	10.6	6.6	1.7	1.4E+7 [c]		4.2	45.1
11-12-2014	NA	NA	NA	4.0	4.4	0.7	NA		NA	NA
12-12-2014	126.5	NA	2.2	5.6	5.0	1.7	2.0E+7 [c]		5.9	44.7
13-12-2014	83.1	14.6	0.9	7.8	3.8	1.8	2.0E+7 [c]		5.2	43.5
16-12-2014	62.4	NA	1.5	6.8	22.4	1.4	1.3E+7 [c]		3.5	44.8
17-12-2014	NA	17.2	NA	25.3	5.1	1.5	NA		3.5	36.0
20-12-2014	154.3	NA	0.9	1.9	7.4	1.1	NA		7.2	59.1
25-12-2014	164.1	NA	2.7	10.6	4.0	0.8	1.4E+7 [c]		7.4	67.8
01-01-2015	NA	NA	NA	7.7	8.1	1.5	NA		3.9	41.1
05-01-2015	145.3	12.4	1.5	5.4	10.1	2.0	4.1E+6 [c]		16.7	71.9
12-01-2015	NA	NA	NA	3.0	18.4	1.0	NA		10.5	65.3
19-01-2015	160.9	45.8	1.3	5.2	5.8	2.1	1.1E+7 [c]		12.1	43.1
05-02-2015	NA	6.8	NA	1.1	7.0	1.6	NA		5.0	66.6
08-02-2015	NA	13.8	NA	1.9	2.8	0.4	NA		6.1	56.0
19-02-2015	129.9	75.9	4.2	7.6	4.6	0.7	6.5E+6 [c]		5.7	65.1
09-03-2015	106.4	23.6	4.1	13.0	10.6	1.0	9.3E+6 [c]		10.8	69.0
10-03-2015	27.1	2.2	1.3	1.6	2.5	0.6	9.2E+6 [c]		4.7	54.7
22-03-2015	117.4	34.3	1.2	2.9	4.7	1.4	9.8E+6 [c]		18.9	23.3
23-03-2015	68.4	10.2	0.6	1.6	9.0	0.7	2.6E+6 [c]		11.7	75.4
24-03-2015	239.8	NA	0.4	12.9	25.5	0.9	4.2E+6 [c]		10.7	46.4
26-03-2015	43.0	14.6	1.2	9.3	7.8	1.0	9.3E+6 [c]		15.5	57.1
08-04-2015	52.6	3.4	0.6	2.8	4.3	1.5	4.3E+6 [c]		9.3	64.8
13-04-2015	92.3	22	1.9	3.4	10.3	2.0	6.2E+6 [c]		14.1	54.9
17-04-2015	34.4	NA	0.5	3.1	5.6	0.8	1.1E+6 [c]		18.4	62.0

21-04-2015	NA	NA	NA	15.3	12.3	1.9	NA		17.5	53.1
30-04-2015	193.0	31.0	1.8	24.8	30.5	2.5	5.6E+6 [c]		22.7	61.0
03-05-2015	NA	NA	0.4	2.6	12.4	2.3	NA		NA	NA
04-05-2015	136.7	68.0	1.1	5.3	9.1	1.8	7.4E+6 [c]		22.2	64.5
12-05-2015	NA	23.8	NA	7.5	11.4	2.2	NA		21.0	55.5
13-05-2015	134.1	45.0	0.5	6.2	27.3	2.9	6.7E+6 [c]		26.1	37.4
16-05-2015	101.4	NA	0.9	6.0	8.4	1.6	4.0E+6 [c]		22.5	32.8
21-05-2015	70.1	3.8	0.7	7.1	18.7	0.8	4.1E+6 [c]		20.1	52.0
03-06-2015	NA	NA	NA	7.4	19.7	NA	NA		24.7	44.6
04-06-2015	NA	NA	NA	1.3	16.3	NA	NA		NA	NA
10-07-2015	114.4	NA	1.3	NA	2.7	1.8	6.5E+6 [c]		25.6	80.7
09-08-2015	NA	7.5	1.1	2.3	7.5	0.7	NA	40.3	29.2	75.0
12-08-2015	NA	NA	NA	NA	50.8	0.8	7.8E+6 [c]	81.7	27.2	72.5
31-08-2015	65.8	NA	1.0	1.1	38.7	1.1	3.0E+6 [c]		27.1	71.7
03-09-2015	112.2	NA	1.4	5.9	33.8	1.6	1.4E+7 [c]		27.0	61.2
06-09-2015	50.9	6.1	0.7	2.1	7.3	1.1	NA		27.3	69.0
08-09-2015	NA	10.3	NA	9.9	6.6	0.9	NA		26.3	62.3
13-09-2015	40.2	10.4	1.7	6.6	11.7	0.9	5.8E+6 [c]		23.5	46.0
17-09-2015	45.7	NA	1.2	29.1	17.2	1.1	6.2E+6 [c]		25.3	59.6
19-09-2015	58.2	NA	0.5	NA	NA	1.0	6.4E+6 [c]		25.6	56.4
21-09-2015	NA	17.9	NA	5.0	9.1	1.1	NA		26.0	57.3
27-09-2015	180.8	NA	1.4	NA	NA	0.9	1.3E+7 [c]		25.9	52.0
10-10-2015	NA	NA	3.9	6.5	10.0	NA	NA		23.8	32.2
11-10-2015	NA	NA	1.8	2.0	12.3	NA	NA		19.9	25.6
12-10-2015	108.2	NA	2.2	3.1	14.9	2.9	1.6E+7 [c]		21.0	33.5
17-10-2015	98.4	13.6	1.9	2.3	10.1	1.0	1.1E+7 [c]		23.1	52.7

28-10-2015	64.7	10.6	1.2	8.8	5.8	1.2	NA		NA	NA
02-11-2015	NA	2.0	NA	4.9	6.7	2.4	NA		NA	NA
04-12-2015	101.2	NA	0.9	20.4	7.4	2.0	1.1E+7 [d]		7.7	35.5
16-12-2015	198.8	28.6	1.9	11.9	6.3	1.3	NA		6.3	28.4
17-12-2015	185.9	21.9	4.7	12.9	3.4	1.5	NA		3.5	37.2
08-01-2016	65.2	10.2	0.7	1.8	7.6	2.7	1.7E+7 [d]		5.6	40.6
23-01-2016	96.1	17.7	3.3	8.1	12.3	1.5	1.0E+7 [d]		-2.4	41.5
24-01-2016	66.6	6.3	1.7	3.3	7.6	1.3	6.8E+6 [d]		-6.3	34.1
25-01-2016	105.8	NA	1.4	1.8	17.9	2.4	1.0E+7 [d]		0.1	31.8
06-02-2016	NA	25.0	NA	6.5	14.5	1.9	1.1E+7 [d]		4.9	37.1
07-02-2016	188.8	7.6	2.2	4.9	25.2	2.4	1.4E+7 [d]		8.2	28.9
08-02-2016	51.6	8.6	1.6	16.7	3.0	2.3	1.2E+7 [d]		13.8	26.1
10-02-2016	26.5	16.8	1.2	10.6	NA	1.2	9.8E+6 [d]		17.6	47.9
15-02-2016	294.8	36	5.0	5.6	11.0	1.7	1.1E+7 [c]		2.9	35.9
16-02-2016	163.4	11.5	2.3	10.0	7.8	1.8	NA		6.7	34.6
20-02-2016	NA	NA	NA	7.6	6.4	1.8	NA		9.9	29.9
24-02-2016	87.4	NA	3.9	2.4	7.3	1.3	5.2E+6 [c]		7.3	49.8

[a] averaged values between the beginning and the peak time for each event.

[b] averaged CS values obtained from the same time range as that for $GR_{<3nm}$ of each event.

[c] averaged sulfuric acid concentrations calculated with the proxy method between the beginning and the peak time for each event.

[d] averaged sulfuric acid concentrations measured between the beginning and the peak time for each event.

NA: Not Available.

Table S2. Mass list of identified species detected by CI-APi-TOF.

ID	Ion formula	Mass to charge (Th)	Remarks
1	$C_2HO_4^-$	88.9880	
2	SO_4^-	95.9522	Sulfur-oxygen compounds
3	HSO_4^-	96.9601	Sulfur-oxygen compounds
4	$C_3H_3O_4^-$	103.0037	
5	SO_5^-	111.9472	Sulfur-oxygen compounds
6	$C_6H_4NO_3^-$	138.0197	
7	$SO_3 \cdot NO_3^-$	141.9452	Sulfur-oxygen compounds
8	$C_2H_2O_4 \cdot NO_3^-$	151.9837	
9	$SO_4 \cdot NO_3^-$	157.9401	Sulfur-oxygen compounds
10	$H_2SO_4 \cdot NO_3^-$	159.9557	Sulfur-oxygen compounds
11	$C_3H_4O_4 \cdot NO_3^-$	165.9993	
12	IO_3^-	174.8898	
13	$HSO_5 \cdot NO_3^-$	174.9428	Sulfur-oxygen compounds
14	$C_4H_6O_4 \cdot NO_3^-$	180.0150	
15	$H_2SO_4 \cdot HSO_4^-$	194.9275	Sulfur-oxygen compounds
16	$C_6H_5NO_3 \cdot NO_3^-$	201.0153	
17	$SO_3 \cdot HNO_3 \cdot NO_3^-$	204.9408	Sulfur-oxygen compounds
18	$C_7H_7NO_3 \cdot NO_3^-$	215.0310	
19	$SO_4 \cdot HNO_3 \cdot NO_3^-$	220.9357	Sulfur-oxygen compounds
20	$C_4H_4O_7 \cdot NO_3^-$	225.9841	
21	$C_5H_3O_6N \cdot NO_3^-$	234.9844	
22	$C_6H_4O_5N_2 \cdot NO_3^-$	246.0004	
23	$IONO_2 \cdot NO_3^-$	250.8807	
24	$C_6H_5NO_3 \cdot HNO_3 \cdot NO_3^-$	264.0110	
25	$C_9H_8O_6 \cdot NO_3^-$	274.0205	
26	$C_7H_7NO_3 \cdot HNO_3 \cdot NO_3^-$	278.0266	
27	$C_{10}H_{10}O_6 \cdot NO_3^-$	288.0568	
28	$C_4H_4O_7 \cdot HNO_3 \cdot NO_3^-$	288.9797	
29	$(H_2SO_4)_2 \cdot HSO_4^-$	292.8949	Sulfur-oxygen compounds
30	$HSO_5 \cdot H_2SO_4 \cdot HSO_4^-$	307.8820	Sulfur-oxygen compounds
31	$C_6H_4O_5N_2 \cdot HNO_3 \cdot NO_3^-$	308.9960	
32	$C_{11}H_{10}O_7 \cdot NO_3^-$	316.0310	
33	$(C_2H_7N) \cdot (H_2SO_4)_2 \cdot HSO_4^-$	337.9527	
34	$C_{11}H_{11}O_8N \cdot NO_3^-$	347.0368	
35	$C_7H_{13}O_{11}N \cdot NO_3^-$	349.0372	
36	$C_{14}H_{14}O_8 \cdot NO_3^-$	372.0572	
37	$C_9H_{15}O_{11}N \cdot NO_3^-$	375.0529	
38	$(C_2H_7N)_2 \cdot (H_2SO_4)_2 \cdot HSO_4^-$	383.0106	
39	$C_{15}H_{16}O_8 \cdot NO_3^-$	386.0729	
40	$C_{14}H_{15}O_8N \cdot NO_3^-$	387.0681	
41	$C_{14}H_{14}O_9 \cdot NO_3^-$	388.0522	
42	$(H_2SO_4)_2 \cdot HSO_4^-$	390.8622	Sulfur-oxygen compounds
43	$C_{15}H_{17}O_8N \cdot NO_3^-$	401.0838	
44	$C_{11}H_{16}O_{12} \cdot NO_3^-$	402.0525	
45	$C_{14}H_{15}O_9N \cdot NO_3^-$	403.0630	
46	$C_{14}H_{17}O_9N \cdot NO_3^-$	405.0787	
47	$C_{12}H_{19}O_{11}N \cdot NO_3^-$	415.0842	

48	$C_{15}H_{17}O_9N \cdot NO_3^-$	417.0787	
49	$C_{10}H_{16}O_{14} \cdot NO_3^-$	422.0424	
50	$(C_2H_7N) \cdot (H_2SO_4)_3 \cdot HSO_4^-$	435.9201	
51	$C_{13}H_{21}O_{12}N \cdot NO_3^-$	445.0947	
52	$(C_2H_7N)_2 \cdot (H_2SO_4)_3 \cdot HSO_4^-$	480.9779	

References and notes:

39. Y. Ma, X. Xu, W. H. Song, F. Geng, L. Wang, Seasonal and diurnal variations of particulate organosulfates in urban Shanghai, China. *Atmos. Environ.* **85**, 152-160 (2014). doi: 10.1016/j.atmosenv.2013.12.017

40. L. Wang, H. Du, J. M. Chen, M. Zhang, X. Huang, H. Tan, L. Kong, F. Geng, Consecutive transport of anthropogenic air masses and dust storm plume: Two case events at Shanghai, China. *Atmos. Res.* **127**, 22-33 (2013). doi:10.1016/j.atmosres.2013.02.011

41. X. K. Wang, S. Rossignol, Y. Ma, L. Yao, M. Y. Wang, J. M. Chen, C. George, L. Wang, Molecular characterization of atmospheric particulate organosulfates in three megacities at the middle and lower reaches of the Yangtze River. *Atmos. Chem. Phys.* **16**, 2285-2298 (2016). doi:10.5194/acp-16-2285-2016

42. J. Vanhanen, J. Mikkilä, K. Lehtipalo, M. Sipilä, H. E. Manninen, E. Siivola, T. Petäjä, M. Kulmala, Particle size magnifier for nano-CN detection. *Aerosol Sci. Technol.* **45**, 533-542 (2011). doi:10.1080/02786826.2010.547889

43. K. Lehtipalo, J. Leppä, J. Kontkanen, J. Kangasluoma, A. Franchin, D. Wimmer, S. Schobesberger, H. Junninen, T. Petäjä, M. Sipilä, J.Mikkilä, J. Vanhanen, D. R. Worsnop, M. Kulmala, Methods for determining particle size distribution and growth rates between 1 and 3 nm using the Particle Size Magnifier. *Boreal Environ. Res.* **19**, 215-236 (2014).

44. S. Mirme, A. Mirme, The mathematical principles and design of the NAIS - a spectrometer for the measurement of cluster ion and nanometer aerosol size distributions. *Atmos. Meas. Tech.* **6**, 1061-1071 (2013). doi:10.5194/amt-6-1061-2013

45. H. E. Manninen, S. Mirme, A. Mirme, T. Petäjä, M. Kulmala, How to reliably detect molecular clusters and nucleation mode particles with Neutral cluster and Air Ion Spectrometer (NAIS). *Atmos. Meas. Tech.* **9**, 3577-3605 (2016). doi:10.5194/amt- 9-3577-2016

46. H. E. Manninen, A. Franchin, S. Schobesberger, A. Hirsikko, J. Hakala, A. Skromulis, J. Kangasluoma, M. Ehn, H. Junninen, A. Mirme, S. Mirme, M. Sipilä, T. Petäjä, D. R. Worsnop, M. Kulmala, Characterisation of corona-generated ions used in a Neutral cluster and Air Ion Spectrometer (NAIS). *Atmos. Meas. Tech.* **4**, 2767-2776 (2011). doi:10.5194/amt-4-2767-2011

47. R.Wagner, H. E. Manninen , A. Franchin , K. Lehtipalo, S. Mirme, G. Steiner, T. Petäjä, M. Kulmala, On the accuracy of ion measurements using a Neutral cluster and Air Ion Spectrometer. *Boreal Environ. Res.* **21**, 230-241 (2016).

48. H. Junninen, M. Ehn, T. Petäjä, L. Luosujärvi, T. Kotiaho, R. Kostiainen , U. Rohner, M. Gonin , K. Fuhrer, M. Kulmala, D. R. Worsnop, A high-resolution mass spectrometer to measure atmospheric ion composition. *Atmos. Meas. Tech.* **3**, 1039-1053 (2010). doi:10.5194/amt-3-1039-2010

49. F. L. Eisele, D. Tanner, Measurement of the gas-phase concentration of H_2SO_4 and methane sulfonic-acid and estimates of H_2SO_4 production and loss in the atmosphere. *J Geophys Res-Atmos* **98**, 9001-9010 (1993). doi:10.1029/93JD00031

50. T. H. Bertram, J. R. Kimmel, T. A. Crisp, O. S. Ryder, R. L. N. Yatavelli, J. A. Thornton, M. J. Cubison, M. Gonin, D. R. Worsnop, A field-deployable, chemical ionization time-of-flight mass spectrometer. *Atmos. Meas. Tech.* **4**, 1471-1479 (2011). doi:10.5194/amt-4-1471-2011

51. J. Zheng, D. S. Yang, Y. Ma, M. D. Chen, J. Cheng, S.Z. Li, M. Wang. Development of a new corona discharge based ion source for high resolution time-of-flight chemical ionization mass spectrometer to measure gaseous H_2SO_4 and aerosol sulfate. *Atmos. Environ.* **119**, 167-173, (2015). doi: 10.1016/j.atmosenv.2015.08.028

52. S. Mikkonen, S. Romakkaniemi, J. N. Smith, H. Korhonen, T. Petäjä, C. Plass-Duelmer, M. Boy, P. H. McMurry, K. E. J. Lehtinen, J. Joutsensaari, A. Hamed, R. L. Mauldin III, W. Birmili, G. Spindler, F. Arnold, M. Kulmala, A. Laaksonen, A statistical proxy for sulphuric acid concentration. *Atmos. Chem. Phys.* **11**, 11319-11334 (2011). doi: 10.5194/acp-11-11319-2011

53. D. R. Hanson, F. L. Eisele, Measurement of prenucleation molecular clusters in the NH_3, H_2SO_4, H_2O system. *J Geophys Res-Atmos* **107**, AAC 10-1- AAC 10-18 (2002). doi: 10.1029/2001JD001100

54. M. J. McGrath, T. Olenius, I. K. Ortega, V. Loukonen, P. Paasonen, T. Kurtén, M. Kulmala, H. Vehkamäki, Atmospheric Cluster Dynamics Code: a flexible method for solution of the birth-death equations, *Atmos. Chem. Phys.* **12**, 2345-2355 (2012). doi: 10.5194/acp-12-2345-2012

55. M. Kulmala, T. Petäjä, T. Nieminen, M. Sipilä, H. E. Manninen, K. Lehtipalo, M. Dal Maso, P. P. Aalto, H. Junninen, P. Paasonen, I. Riipinen, K. E. Lehtinen, A. Laaksonen, V. M. Kerminen, Measurement of the nucleation of atmospheric aerosol particles. *Nat. protoc.* **7**, 1651-1667 (2012). Medline doi:10.1038/nprot.2012.091

56. K. E. J. Lehtinen, M. Dal Maso, M. Kulmala, V. -M. Kerminen, Estimating nucleation rates from apparent particle formation rates and vice versa: Revised formulation of the Kerminen-Kulmala equation. *J .Aerosol. Sci.* **38**, 988-994 (2007). doi: 10.1016/j.jaerosci.2007.06.009

57. T. Yli-Juuti, T. Nieminen, A. Hirsikko, P. P. Aalto, E. Asmi, U. Hõrrak, H. E. Manninen, J. Patokoski, M. Dal Maso, T. Petäjä, J. Rinne, M. Kulmala, I. Riipinen, Growth rates of nucleation mode particles in Hyytiala during 2003-2009: variation with particle size, season, data analysis method and ambient conditions. *Atmos. Chem. Phys.* **11**, 12865-12886 (2011). doi:10.5194/acp-11-12865-2011

58. T. Nieminen, K. E. J. Lehtinen, M. Kulmala, Sub-10 nm particle growth by vapor condensation - effects of vapor molecule size and particle thermal speed. *Atmos. Chem. Phys.* **10**, 9773-9779 (2010). doi:10.5194/acp-10-9773-2010

59. M. Amanna, I.Bertoka , J. Borken-Kleefelda , J. Cofalaa , C. Heyesa , L. Höglund-Isakssona , Z. Klimonta , B. Nguyena , M. Poschb , P. Rafaja , R. Sandlera , W. Schöppa , F. Wagnera , W. Winiwarter, Cost-effective control of air quality and greenhouse gases in Europe: Modeling and policy applications. *Environ. Modell. Softw.* **26**, 1489-1501, (2011). doi: 10.1016/j.envsoft.2011.07.012